

Mercury's magnetic field in the MESSENGER era

J. Wicht¹ and D. Heyner²

¹Max-Planck Institut für Sonnensystemforschung, Göttingen, Germany,
wicht@mps.mpg.de

²Institut für Geophysik und extraterrestrische Physik, TU Braunschweig, Braunschweig,
Germany

January 19, 2017

Abstract

MESSENGER magnetometer data show that Mercury's magnetic field is not only exceptionally weak but also has a unique geometry. The internal field resembles an axial dipole that is offset to the North by 20% of the planetary radius. This implies that the axial quadrupole is particularly strong while the dipole tilt is likely below 0.8° . The close proximity to the sun in combination with the weak internal field results in a very small and highly dynamic Hermean magnetosphere. We review the current understanding of Mercury's internal and external magnetic field and discuss possible explanations. Classical convection driven core dynamos have a hard time to reproduce the observations. Strong quadrupole contributions can be promoted by different measures, but they always go along with a large dipole tilt and generally rather small scale fields. A stably stratified outer core region seems required to explain not only the particular geometry but also the weakness of the Hermean magnetic field. New interior models suggest that Mercury's core likely hosts an iron snow zone underneath the core-mantle boundary. The positive radial sulfur gradient likely to develop in such a zone would indeed promote stable stratification. However, even dynamo models that include the stable layer show Mercury-like magnetic fields only for a fraction of the total simulation time. Large scale variations in the core-mantle boundary heat flux promise to yield more persistent results but are not compatible with the current understanding of Mercury's lower mantle.

1 Introduction

In 1974 the three flybys of the Mariner 10 spacecraft revealed that Mercury has a global magnetic field. This was a surprise for many scientists since an internal dynamo process was deemed unlikely because of the planet's relative small size and its old inactive surface [Solomon, 1976]. Either the iron core would have already solidified completely or the heat flux through the core-mantle boundary (CMB)

would be too small to support dynamo action. The Mariner 10 measurements also indicated that Mercury's magnetic field is special [Ness et al., 1974]. Being 100 times smaller than the geomagnetic field, it seems too weak to be supported by an Earth-like core dynamo. And though the data were scarce, they nevertheless allowed to constrain that the internal field is generally large scale and dominated by a dipole but possibly also a sizable quadrupole contribution. Both the Hermean field ampli-

tude and its geometry are unique in our solar system.

Mercury is the closest planet to the Sun and therefore subject to a particular strong and dynamic solar wind. Since Mercury's magnetic field is so weak, the solar wind plasma can come extremely close to the planet and may even reach the surface. Mariner 10 data showed that Mercury's magnetosphere is not only much smaller than its terrestrial counterpart but also much more dynamic. Adapted models originally developed for Earth failed to adequately describe the Hermean magnetosphere which therefore remained little understood in the Mariner 10 era [Slavin et al., 2007].

Knowing a planet's internal structure is crucial for understanding the core dynamo process. Mercury's large mean density pointed towards an extraordinary huge iron core and a relatively thin silicate mantle covering only about the outer 25% in radius. Since little more data were available in the Mariner era, the planet's interior properties and dynamics remained poorly constrained.

Solving the enigmas about Mercury's magnetic field and interior were major incentives for NASA's MESSENGER mission [Solomon et al., 2007]. After launch in August 2004 and a first Mercury flyby in January 2008, the spacecraft went into orbit around the planet in March 2011. At the date of writing, more than 2800 orbits have been completed. MESSENGER's orbit is highly eccentric with a periaapsis between 200 to 600 km at 60 to 70° northern latitude and an apoapsis of about 15,000 km altitude. This has the advantage that the spacecraft passes through the magnetosphere on each orbit but complicates the extraction of the internal field component because of a strong covariance of equatorially symmetric and anti-symmetric contributions [Anderson et al., 2012, Johnson et al., 2012]. The trade-off between the dipole and quadrupole field harmonics, that was already a problem with

Mariner 10 data, therefore remains an issue in the MESSENGER era. The situation is further complicated by the fact that the classical separation of external and internal field contributions developed by Gauss [Olsen et al., 2010] does not directly apply at Mercury. It assumes that the measurements are taken in a source free region with negligible electric currents, an assumption not necessarily fulfilled in such a small and dynamic magnetosphere.

In order to nevertheless extract information on the internal magnetic field, the MESSENGER team analysed the location of the magnetic equator where B_ρ , the magnetic field component perpendicular to the planet's rotation axis, passes through zero [Anderson et al., 2011, Anderson et al., 2012]. Since the internal field changes on a much slower time scale than the magnetosphere, the time-averaged location should basically not be affected by the magnetospheric dynamics. The analysis not only confirmed that the Hermean field is exceptionally weak with an axial dipole of only 190 nT but also suggested that the internal field is best described by an axial dipole that is offset by 480 km to the north of the planet's equator [Anderson et al., 2012]. This configuration, that we will refer to as the MESSENGER offset dipole model (MODM) in the following, requires a strong axial quadrupole and a very low dipole tilt, a combination that is unique in our solar system.

This article tries to summarize the new understanding of Mercury's magnetic field in the MESSENGER era at the date of writing. MESSENGER is still orbiting its target and continues to deliver outstanding data that will further improve our knowledge of this unique planet. Section 3 briefly reviews the current knowledge of Mercury's magnetosphere. Section 4 describes recent models for the planet's interior, focussing in particular on the possible core dynamics. The magnetic equator analysis and the offset dipole model MODM are then

discussed in section 4. Explaining the weakness of Mercury’s magnetic field already challenged classical dynamo theory and the peculiar field geometry further raises the bar. Section 5 reanalysis several dynamo model candidates in the light of the new MESSENGER data. Some concluding remarks in section 6 close the paper.

2 Mercury’s internal structure

MESSENGER observations of Mercury’s gravity field [Smith et al., 2012] and Earth-based observations of the planet’s spin state [Margot et al., 2012] provide valuable information on the interior structure. That fact that Mercury is in a special rotational state (Cassini state 1) allows to deduce the polar moment of inertia C from the degree two gravity moments and the planet’s obliquity, the tilt of the spin axis to the orbital normal [Peale, 1969]. The moment of inertia factor $C/(MR_M^2)$, where M is the planet’s total mass and R_M its mean radius, constrains the interior mass distribution. The factor is 0.4 for uniform density and decreases when the mass is increasingly concentrated towards the center. The Hermean value of $C/(MR_M^2) = 0.346 \pm 0.014$ [Margot et al., 2012] indicates a significant degree of differentiation.

The observation of the planet’s 88 day libration amplitude g_{88} , a periodic spin variation in response to the solar gravitational torques on the asymmetrically shaped planet, allows to also deduce the moment of inertia of the rigid outer part C_m . If the iron core is at least partially liquid, C_m is the moment of the silicate shell and thus smaller than C . The Herman value of $C_m/C = 0.431 \pm 0.025$ [Margot et al., 2012] confirms that the core remains at least partially liquid.

In addition to M and R_M the ratios

$C/(MR_M^2)$ and C_m/C provide the main constraints for models of Mercury’s interior [Smith et al., 2012, Hauck et al., 2013]. Note that Rivoldini and Van Hoolst [2013] follow at somewhat different approach, taking into account the possible coupling between the core and the silicate shell. The coupling has the effect that C_m cannot be determined independently of the interior model and Rivoldini and Van Hoolst [2013] therefore directly use g_{88} rather than C_m as a constraint. The updated interior modelling indicates that the core radius is relatively well constrained at 2020 ± 30 km [Hauck et al., 2013] or 2004 ± 39 km [Rivoldini and Van Hoolst, 2013]. This leaves only the outer 16 to 19% of the mean planetary radius $R_M = 2440$ km to the mantle.

Hauck et al. [2013] find a mean mantle density (including the crust) of 3380 ± 200 kg/m³. Measurements of MESSENGER’s X-Ray Spectrometer (XRS) show that the volcanic surface rocks have a low content of iron and other heavier elements [Nittler et al., 2011]. Smith et al. [2012] and Hauck et al. [2013] therefore speculate that a solid FeS outer core layer may be required to explain the mean mantle density. Rivoldini and Van Hoolst [2013], however, argue that the mantle density is not particularly well constrained. Compositions compatible with XRS measurements are well within the allowed solutions and a denser lower mantle layer is not required by the data.

Naturally, information about the core is of particular interest for the planetary dynamo. There is a rough consensus on the mean core density with Hauck et al. [2013] and Rivoldini and Van Hoolst [2013] suggesting 6980 ± 280 kg/m³ and 7233 ± 267 kg/m³, respectively. However, the core composition and the radius of a potential inner core are not well constrained. Admissible interior models cover all inner core radii from zero to very large values with an aspect ratio of about $a = r_i/r_o = 0.9$ [Rivoldini and Van Hoolst, 2013] where r_i

and r_o are the inner and outer core radii, respectively.

An additional constraint on the inner core size relies on the observations of so-called lobate scarps on the planet's surface which are likely caused by global contraction. MESSENGER data based on 21% of the surface suggested a contraction between 1 and 3 km [Di Achille et al., 2012]. This sets severe bounds on the amount of solid iron in Mercury's core because of the density decrease associated with the phase transition of the liquide core alloy. Several thermal evolution models therefore favour a completely liquide core or only a very small inner core [Grott et al., 2011, Tosi et al., 2014]. Recent more comprehensive MESSENGER observations, however, allow for a contraction of up to 7 km. This somewhat releases the constraints [Solomon et al., 2014] though very large inner cores may still be unlikely.

Sulfur has been found in many iron-nickel meteorites and is therefore a prime candidate for the light constituent in Mercury's core. Rivoldini and Van Hoolst [2013] consider iron-sulfur core alloys and find a likely bulk sulfur concentration of 4.5 ± 1.8 wt%. Since this composition lies on the iron rich side of the eutectic, iron crystalizes out of the liquid when the temperature drops below the melting point. Where this happens first depends on the form of the melting curve and the adiabat describing core conditions.

Since Mercury's mantle is so thin it has likely cooled to a point where mantle convection is very sluggish or may have stopped altogether [Grott et al., 2011, Michel et al., 2013, Tosi et al., 2014]. The heat flux through the core-mantle boundary is thus likely subadiabatic and therefore too low to support a core dynamo driven by thermal convection alone. The required additional driving power may then either be provided by a growing inner core or by an iron snow zone. The solid inner core starts to grow as soon as the adiabat crosses the melt-

ing curve in the planetary center. Since the solid iron phase can incorporate only a relatively small sulfur fraction, most of the sulfur is expelled at the inner core front and drives compositional convection. The latent heat released upon iron solidification provides additional thermal driving power. Contrary to the situation for Earth, freezing could also start at the core-mantle boundary (CMB) because of the lower pressures in Mercury's core. The iron crystals would then precipitate or snow into the center and remelt when encountering temperatures above the melting point at a depth r_m . This process leaves a sulfur enriched lighter residuum in the layer $r > r_m$. As the planet cools, r_m decreases and a stabilizing sulfur gradient is established that follows the liquidus curve and covers the whole snow zone $r > r_m$ [Hauck et al., 2006]. Since the heat flux through the CMB is likely subadiabatic today, thermal effects will also suppress rather than promote convection in the outer part of Mercury's core. A stably stratified layer underneath the planet's core mantle boundary and probably extending over the whole iron snow region therefore seems likely. The liquid iron entering the layer below r_m serves as a compositional buoyancy source. The latent heat being released in the iron snow zone diffuses to the core mantle boundary. Today's low CMB heat flux implies that this can be achieved by a relatively mild temperature gradient.

The possible core scenarios are illustrated in fig. (1) with melting curves for different sulfur concentrations and core adiabats with CMB temperatures in the range between 1600 and 2000 K suggested by interior [Rivoldini and Van Hoolst, 2013] and thermal evolution models [Grott et al., 2011, Michel et al., 2013, Tosi et al., 2014]. Data on the melting behaviour of iron-sulfur alloys are few and the melting curves shown in fig. (1) therefore rely on simple parametrizations [Rivoldini et al., 2011]. The adiabats have been calculated by Rivoldini and

Van Hoolst [2013]. Mercury’s core pressure is only grossly constrained, with CMB pressures in the range 4 – 7 GPa and central pressures in the range 30 – 45 GPa [Hauck et al., 2013]. We adopt a central pressure of 40 GPa here. Fig. (1) suggests that iron starts to solidify in the center for an initial sulfur concentrations below about 4 wt%. Sulfur released from the inner core boundary increases the concentration in the liquid core over time and thereby slows down the inner core growth and delays the onset of iron snow. For an initial sulfur concentration beyond 4 wt% iron solidification starts with the CMB snow regime. A convective layer that is enclosed by a solid inner core and a stably stratified outer iron snow layer seems possible for sulfur concentrations between about 2.5 and 7 wt%. For sulfur concentration beyond 7 wt% an inner core would only grow when the snow zones extends through the whole core and the snow starts to accumulate in the center.

The adiabats and thin red lines in fig. (1) illustrate the evolution for an initial sulfur concentration of 3 wt%. For the hot (red) adiabat with $T_{cmb} = 2000$ K neither inner core growth nor iron snow would have started and there would be no dynamo. When the temperature drops, iron starts to solidify first at the center. For a CMB temperature of $T_{cmb} = 1910$ K (solid green adiabat), the inner core has already grown to a radius of about 600 km while the outer snow layer is only about 160 km thick. The sulfur released upon inner core growth has increased the bulk concentration in the liquid part of the core to 3.4 wt% (first thin red line from the top). The decrease in the sulfur abundance due to the remelting of iron snow has not been taken into account in this model. When the CMB temperature has dropped to $T_{cmb} = 1890$ K (dashed green adiabat) the inner core and snow layer have grown by a comparable amount while the sulfur concentration has increased to 4.4 wt% (second

thin red line from the top). At $T_{cmb} = 1750$ K (grey) there remains only a relatively thin convective layer between the inner core boundary at $r_i = 1440$ km and the lower boundary of the outer snow layer at $r_m = 1650$ km. For the coldest adiabat shown in fig. (1) with $T_{cmb} = 1890$ K (blue) only the outer 300 km of the core remain liquid but belong to the iron snow zone so that no dynamo seems possible.

Additional sometimes complex scenarios have been discussed in the context of Ganymede by Hauck et al. [2006] and may also apply at Mercury since the iron cores of both bodies cover similar pressure ranges. For example, fig. (1) illustrates a kink in the melting curve for pressures around 21 GPa and compositions larger than 5 wt% sulfur. This could lead to a double snow regime where not only the very outer part of the core precipitates iron but also an intermediate layer around 21 GPa. This possibility has been explored in a dynamo model by Vilim et al. [2010] that we will discuss in section 2. Since the kink is not very pronounced, however, such a double snow dynamo would not be very long lived.

Another interesting scenario unfolds when the light element concentration lies on the S-rich side of the eutectic. Under these conditions, FeS rather than Fe would crystalize out when the temperature drops below the FeS melting curve. Since FeS is lighter than the residuum fluid, the crystals would rise towards the core-mantle boundary. However, eutectic or even higher sulfur concentrations cannot represent bulk conditions since it would be difficult to match Mercury’s total mass [Rivoldini et al., 2011]. Inner core growth would increase the sulfur concentration in the remaining fluid over time but never beyond the eutectic point. This has likely not been reached in Mercury because the eutectic temperature of 1200 – 1300 K [Rivoldini et al., 2011] is significantly lower than today’s CMB temperature suggested by thermal evolution [Grott et al.,

2011, Tosi et al., 2014] and interior models [Rivoldini and Van Hoolst, 2013].

An alternative explanation for a locally high sulfur concentration was suggested by the XRS observations. The low Fe but large S abundance in surface rocks indicates that Mercury's core could have formed at strongly reducing conditions. This promotes a stronger partitioning of Si into the liquid iron phase leading to a ternary Fe-Si-S core alloy [Malavergne et al., 2010]. Experiments have shown that Si and S are immiscible for pressures below 15 GPa [Morard and Katsura, 2010] which is the pressure range in the outer part of Mercury's core. However, the immiscibility only happens for sizable Si and S concentrations. Experiments by Morard and Katsura [2010], for example, demonstrate that at 4 GPa and 1900 K abundances of 6 wt% S and 6 wt% Si are required to trigger the immiscibility and lead to the formation of a sulfur rich phase with a composition of about 25 wt% S. For FeS crystallization to play a role at today's CMB temperatures, the sulfur rich phase should lie significantly to the right of the eutectic where the FeS melting temperature increases with light element abundance. Thus even higher S and Si contributions are required but seem once more difficult to reconcile with the planet's total mass [Rivoldini and Van Hoolst, 2013]. Since Si partitions much more easily into the solid iron phase than sulfur, its contribution to compositional convection and the stabilization of the snow zone is significantly weaker.

Several numerical studies in the context of Earth and Mars have shown that the CMB heat flux pattern can have a strong effect on the dynamo mechanism (see e.g. Wicht et al. [2011a] and Dietrich and Wicht [2013] for overviews). Like the mean heat flux out of the core, this pattern is controlled by the lower mantle structure. The Martian dynamo ceased about 4 Gyr ago but has left its trace in form of a strongly magnetized crust. The fact that the

magnetization is much stronger in the southern than in the northern hemisphere could reflect a special configuration of the planet's ancient dynamo. Impacts or large degree mantle convection may have significantly decreased the heat flux through the northern CMB and therefore weakened dynamo action in this hemisphere [Stanley et al., 2008, Amit et al., 2011, Dietrich and Wicht, 2013]. Mercury's magnetic field is distinctively stronger in the northern than in the southern hemisphere and it seems attractive to invoke an increased northern CMB heat flux as a possible explanation.

Clues about the possible pattern may once more come from MESSENGER observations. A combination of gravity and altimeter data allowed to estimate the crustal thickness in the northern hemisphere. On average, the crust is about 50 km thicker around the equator than around the pole [Smith et al., 2012] which points towards more lava production and thus a hotter mantle at lower latitudes. This is consistent with the fact that the northern lowlands are filled by younger flood basalts since melts more easily penetrate a thinner crust [Denevi et al., 2013]. Missing altimeter data and the degraded precision of gravity measurements does not allow to constrain the crustal thickness in the southern hemisphere. The lack of younger flood basalts, however, could indicate a thicker crust and hotter mantle. Since a hotter mantle would reduce the CMB heat flux, these ideas indeed translate into a pattern with increased flux at higher northern latitudes. However, Mercury's volcanism ceased more than 3.5 Gyr ago and today's thermal mantle structure may look completely different. Even simple thermal diffusion should have eroded any asymmetry over such a long time span. Thermal evolution simulations show that at least the lower part of the mantle may still convect today [Smith et al., 2012, Tosi et al., 2014] which would change the structure on much shorter time scales. Since the active

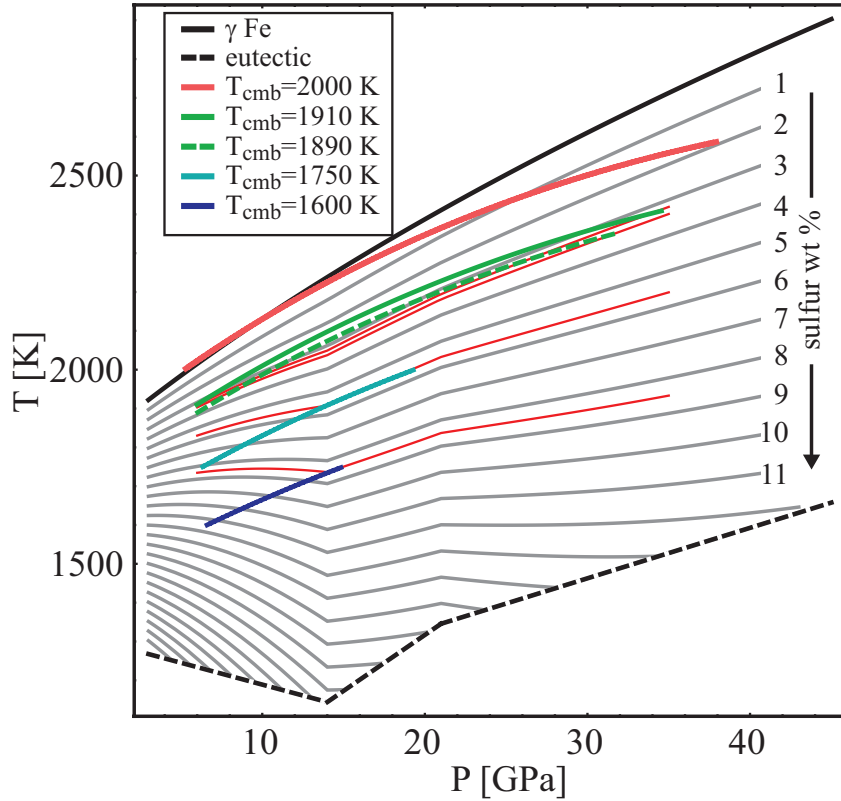


Figure 1: Melting curves for different initial sulfur concentrations and possible Mercury adiabats for different temperatures shown as thick red, green, turquoise, and blue lines. Thin red lines from top to bottom show the melting curves for the convecting part of the core for an initial sulfur concentration of 3 wt% and a core state described by the solid green, dashed green, gray, and blue adiabats. The thick solid black line shows the melting curve for pure iron while the thick dashed black line shows the eutectic temperature. The figure, provided by Attilio Rivoldini, and has been adapted from Rivoldini et al. [2011] to include the Mercury core adiabats calculated in Rivoldini and Van Hoolst [2013]. A central pressure of 40 GPa is assumed for Mercury but the adiabats are only drawn in the liquid part of the core.

shell is so thin, the pattern would be rather small scale without any distinct north/south asymmetry.

Because of Mercury’s 3:2 spin-orbit resonance, the high eccentricity of the orbit, and the very small obliquity the time averaged insolation pattern shows strong latitudinal and longitudinal variations. Williams et al. [2011] calculates that the mean polar temperature can be 200 K lower than the equatorial. Longitudinal variations show two maxima that are about 100 K hotter than the minima at the equator. If Mercury’s mantle convection has ceased long ago, the respective pattern may have diffused into the mantle and could determine the CMB heat flux variation. Higher than average flux at the poles and a somewhat weaker longitudinal variation would be the consequence. We discuss the impact of the CMB heat flux pattern on the dynamo process in section 2.

3 Mercury’s external magnetic field

Planetary magnetospheres are the result of the interaction between the planetary magnetic field and the impinging solar wind plasma. Because of Mercury’s weak and asymmetric magnetic field and the position close to the Sun, the Hermean and terrestrial magnetospheres differ fundamentally. Mercury experiences the most intense solar wind of all solar-system planets. Under average conditions, the ratio of the solar wind speed and the Alfvén velocity, called the Alfvénic Mach-number, is comparable to the terrestrial one. With values of 6.6 for Mercury [Winslow et al., 2013] and 8 for Earth, the solar wind plasma is super-magnetosonic at both planets, i.e. the medium propagates faster than magnetic disturbances and a bow shock therefore forms in front of the magnetosphere. Because of the weak Hermean magnetic field, the sub-solar point of the bow shock is located

rather close to the planet at an average position of only 1.96 planetary radii [Winslow et al., 2013] compared to 14 planetary radii for Earth.

Behind the bow shock, the cold solar wind plasma is heated up and interacts with the planetary magnetic field, thereby creating the magnetosphere. To first order, the planetary fieldlines form closed loops within the dayside magnetosphere and a long tail on the nightside. The outer boundary of the magnetosphere, the magnetopause, is located where the pressure of the shocked solar wind and the pressure of the planetary magnetic field balance. The solar wind ram pressure, on average 14.3 nPa at Mercury [Winslow et al., 2013], is an order of magnitude higher than at Earth while the magnetic field is two orders of magnitude weaker. Like the bow shock, the magnetopause is therefore located much closer to the planet at Mercury than at Earth with mean standoff distances of about 1.45 [Winslow et al., 2013] and 10 planetary radii, respectively. Both the Hermean magnetosphere and magnetosheath, the region between bow shock and magnetopause, are thus much smaller than the terrestrial equivalents in relative and absolute terms.

Fig. (2) shows the current density in a numerical hybrid simulation that models the solar wind interaction with the planet [Müller et al., 2012]. The location of the bow shock and the magnetosphere can be identified via the related current systems. Along a spacecraft trajectory these boundaries can be identified by the related magnetic field changes. Fig. (3) shows MESSENGER magnetic field measurements for a relatively quiet orbit (orbit number 14) where both the bow shock and the magnetopause can be clearly classified on both sides of the planet.

Another important element of the magnetosphere is the neutral current sheet which is responsible for the elongated nightside magnetotail and separates the northern and south-

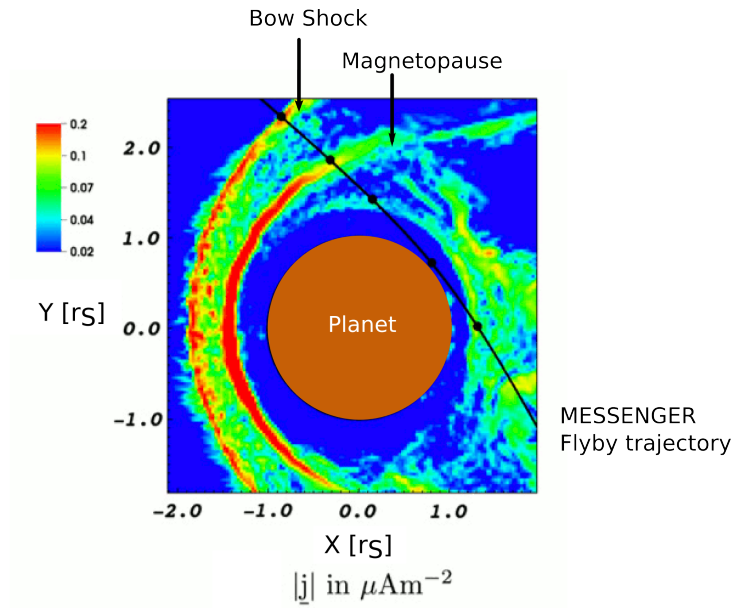


Figure 2: Electrical currents in a numerical simulation of the Hermean magnetosphere. The amplitude of the current density j is color-coded. An equatorial cross section is shown in a coordinate system where X points towards the Sun (negative solar wind direction) and the Y -axis lies in the Hermean ecliptic. The bow shock standing in front of the planet slows down the solar wind. The magnetopause is the outer boundary of the magnetosphere. The neutral current sheet is located in the nightside of the planet. An arc of electrical current visible close to the flyby trajectory (January 14, 2008) could be interpreted as a partial ring current. This figure is a snapshot from a solar wind hybrid simulation and is adapted from Müller et al. [2012].

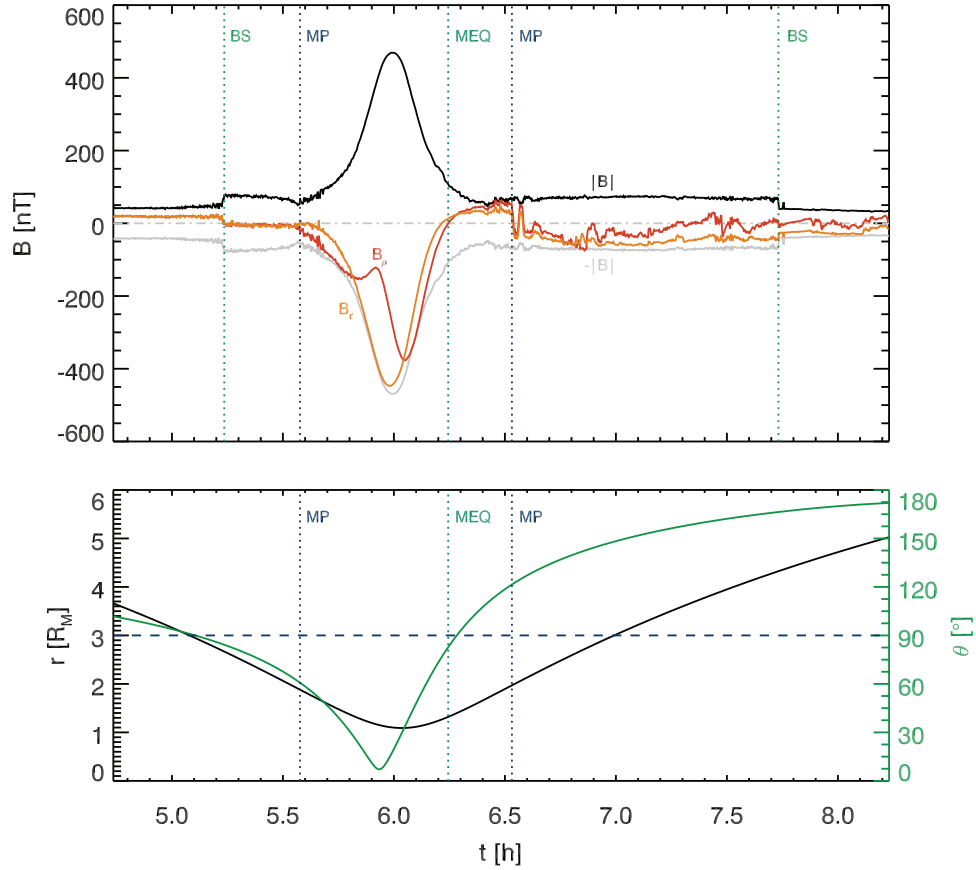


Figure 3: Magnetic field data recorded by the MESSENGER magnetometer (10s average) during orbit 14 on the DOY 84 in 2011. The *upper panel*, shows the time series of the absolute magnetic field $|B|$ (black), the negative absolute field (grey), the radial component B_r (green), and the component B_ρ perpendicular to the rotation axis. Time is measured in hours since the last apocenter passage. The plasma boundaries are marked with vertical dashed lines (BS: bow shock, MP: magnetopause). The location where B_ρ vanishes defines the magnetic equator (MEQ). The *lower panel* shows the planetocentric distance r and the co-latitude θ . The data are taken from the Planetary Data System / Planetary Plasma Interactions Node.

ern magnetotail lobes. Johnson et al. [2012] report, that the sheet starts at $1.41 R_M$, where R_M is the mean Hermean radius, which is approximately the standoff distance of the day-side magnetopause. Roughly the same proportion is also found at Earth.

The locations of bow shock, magnetopause and neutral current sheet is not stationary but vary in time. The density of the average solar wind decreases with distance r_S to the Sun like $1/r_S^2$. Since Mercury orbits the Sun on a highly elliptical orbit (ellipticity: 0.21) the local solar wind pressure varies significantly on the orbital time-scale of 88 days. The solar wind characteristics also changes constantly on much shorter time scales because of spatial inhomogeneities due to, for example, coronal-mass ejections. As a result, the Hermean magnetosphere is very dynamic. And since the magnetosphere is so small, the magnetic disturbance also propagate deep into the magnetosphere and impede the separation of the field into internal and external contributions [Glassmeier et al., 2010]. Reconnection processes in the magnetotail are another source for variations in the Hermean magnetosphere [Slavin et al., 2012].

The Hermean and terrestrial magnetospheres differ in several additional aspects. Mercury’s surface temperature can reach several hundred Kelvin which means that the planet’s gravitational escape velocity of 4.3 km/s can easily be reached thermally. The thermal escape rate is therefore significant and the remaining atmosphere too thin to form an ionosphere. At Earth, the ionosphere hosts substantial current systems that significantly affect the magnetospheric dynamics, for example magnetic sub-storms. Field-aligned currents that close via the ionosphere at Earth must close within the magnetospheric plasma or the planetary body at Mercury [Janhunen and Kallio, 2004].

When the planetary magnetic field on the in-

side of the magnetopause is nearly antiparallel to the magnetosheath field on the outside, the respective fieldlines can reconnect. This typically happens when the interplanetary magnetic field has a component parallel to the planetary field. The reconnected fieldlines are advected tail-wards by the solar wind, which drives a global scale magnetospheric convection loop that ultimately replenishes the day-side field (Dungey-Cycle). Due to the small size of the Hermean magnetosphere, the typical timescale of this plasma circulation is only about 1 – 2 minutes compared to 1 h at Earth [Slavin et al., 2012] which demonstrates that the Hermean magnetosphere can adapt much faster to changing solar wind conditions. The rate of reconnection, measured by the relative amplitude of the magnetic field component perpendicular to the magnetopause, is about 0.15 at Mercury and thus 3 times higher than at Earth [Dibraccio et al., 2013].

Charged particles that are trapped inside the magnetosphere and drift around the planet in azimuthal direction form a major magnetospheric current system at Earth, the so-called ring current. The drift is directed along isocontours of the magnetic field strength. However, since internal and magnetospheric field can reach comparable values these contours close via the magnetopause at Mercury, as is illustrated in fig. (4). At Earth, the planetocentric distance $R_{rc,E}$ of the ring current is about four times the terrestrial radius. When assuming that the position scales linearly with the planetary dipole moment, the distance can be rescaled to the Hermean situation by

$$R_{rc,M} = R_{rc,E} \frac{m_M}{m_E} \approx 820\text{km} \quad (1)$$

where m_M and m_E are the dipole moments of Mercury and Earth, respectively. The ring current would thus clearly lie below Mercury’s surface. Hybrid simulations by Müller et al. [2012] indicate that the solar wind protons entering

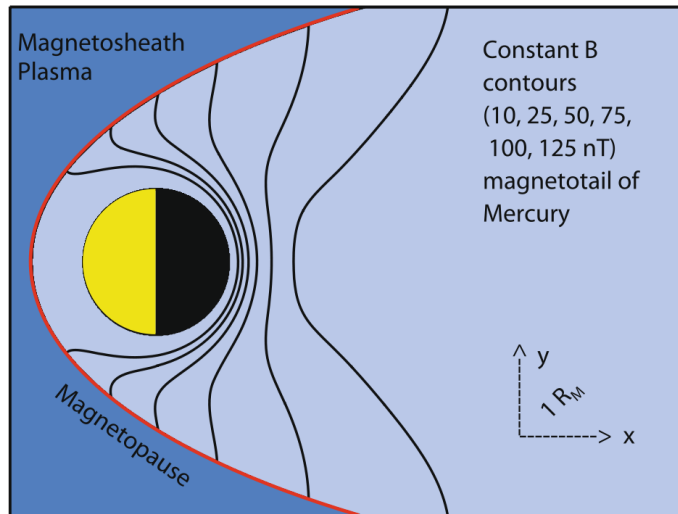


Figure 4: Equatorial isocontours of the total magnetic field in a Hermean model magnetosphere. The magnetopause is shown as a red line and the planet as a sphere. Figure from Baumjohann et al. [2010].

the magnetosphere can drift roughly half-way around the planet before being lost to the magnetopause, as is illustrated in fig. (2). This could be interpreted as a partial ring current. The protons create a diamagnetic current that locally decreases the magnetic field.

Because MESSENGER delivers only data from one location at a time inside a very dynamic magnetosphere, it is not only challenging to separate internal from external field contributions but also temporal from spatial variations. Numerical simulations for the solar wind interaction with the planetary magnetic field, like the hybrid simulation used to investigate the partial ring current (see fig. (2)), can improve the situation by constraining the possible spatial structure for a given solar wind condition. However, as these codes are numerically very demanding, it becomes impractical to perform simulation for all the different conditions possibly encountered by MESSENGER. A more practical approach is to use simplified models where a few critical proper-

ties like the shape of the magnetopause and the strength and shape of the neutral current sheet are described with a few free parameters. Johnson et al. [2012] demonstrate how the parameters can be fitted to MESSENGER's accumulated magnetic field data to derive a model for the time averaged magnetosphere.

The offset of Mercury's magnetic field by 20% of the planetary radius to the north can cause an equatorial asymmetry of the planet's exosphere. Ground-based observations of sodium emission lines suggest that there is more sodium released from the southern than the northern planetary surface. Mangano et al. [2013] argue that precipitating solar wind protons are the main player in the sodium release and more likely reach the southern surface where the magnetic field is weaker.

The Hermean magnetosphere resembles its terrestrial counterpart in several aspects but there are also huge differences. Mercury's magnetosphere is much smaller and significantly more dynamic, responding much faster

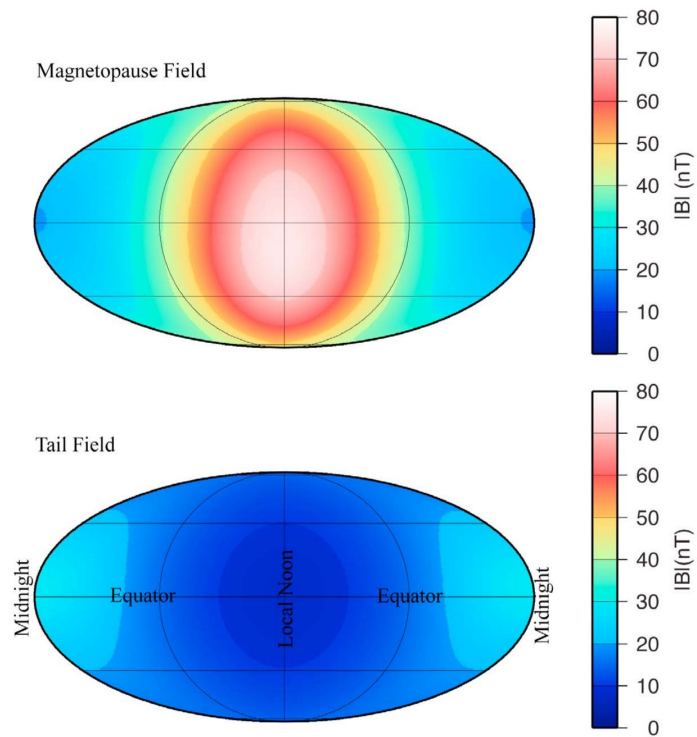


Figure 5: External fields from the paraboloid model based on measurements of the MESSENGER mission at the planetary surface. *Top panel:* amplitude of the magnetopause field. *Bottom panel:* amplitude of the neutral sheet magnetic field. Figure from Johnson et al. [2012].

to changing solar wind conditions. While the external field contributions are orders of magnitude smaller than internal contributions at Earth, they can become comparable at Mercury (see fig. (5)). This lead Glassmeier et al. [2007] to investigate the long-term effect of the external field on the internal dynamo process, as we will further discuss in section 5.

4 Mercury’s internal magnetic field

The difficulties in separating internal and external field and the strong covariance of different spherical harmonic contributions caused by the highly elliptical orbit complicate a classical field modelling with Gaussian coefficients for Mercury [Anderson et al., 2011]. Instead, the MESSENGER magnetometer team analysed the location of the magnetic equator to indirectly deduce the internal field. The magnetic equator is the point where the magnetic field component B_ρ perpendicular to the planetary rotation axis vanishes. Changing solar wind conditions lead to variations in the equator location on different time scales from seconds to months but should average out over time, at least as long as the planetary body itself has no first order impact on the magnetospheric current system. The mean location of the magnetic equator is then primarily determined by the internal field.

Anderson et al. [2012] analysed the magnetic equator for 531 descending orbits with altitudes between 1000 and 1500 km and 120 ascending orbits with altitudes between 3500 and 5000 km. They find that the equator crossings are confined to a relatively thin band offset by about $Z = 480$ km to the north of the planet’s equator. We adopt a planet-centered cylindrical coordinate system here where ρ and z are the coordinates perpendicular to and along the rotation axis, respectively, and Φ is the

longitude. Anderson et al. [2012] minimized the effects of solar wind related magnetic field variations by considering a mean where each equator location is weighted with the inverse of the individual standard error σ . This procedure yields a mean offset of $\bar{Z}_d = 479$ km with a standard deviation of $\Delta\bar{Z}_d = 46$ km for the descending orbits. The mean three standard error in determining the individual equator crossings is $3\bar{\sigma}_d = 24$ km. Because of the increased solar wind influence and the closer proximity to the magnetosphere, the magnetic equator is less well defined for the ascending orbits with $\bar{Z}_a = 486$ km, $\Delta\bar{Z}_a = 270$ km, and $3\bar{\sigma}_a = 86$ km (see table 1 in Anderson et al. [2012]).

These observations suggest that the offset of the magnetic equator has a constant value of 480 km independent of the distance to the planet. Such a configuration can readily be explained by an internal axial dipole that is offset by 480 km to the North of the equatorial plane. This translates into an infinite sum of axisymmetric Gaussian field coefficients g_ℓ in the classical planet-centered representation with

$$g_{\ell 0} = \ell g_{10} \mathcal{Z}^{\ell-1} , \quad (2)$$

where $\mathcal{Z} = Z/R_M$ is the normalized offset and ℓ the spherical harmonic degree [Bartels, 1936, Alexeev et al., 2010]. Note that all contributions have the same sign. In the Gaussian representation the planetary surface field is expanded into spherical surface harmonics $Y_{\ell m}$ of degree ℓ and order m [Olsen et al., 2010]. The coefficients $g_{\ell m}$ and $h_{\ell m}$ express the $\cos(m\phi)$ and $\sin(m\phi)$ dependence for a given degree ℓ . Only coefficients $g_{\ell 0}$ contribute to an axisymmetric field.

Anderson et al. [2012] report that coefficients up to $\ell = 4$ suffice to explain the mean magnetic equator locations in the MESSENGER offset dipole model (MODM). To illustrate the characteristics of MODM, we experi-

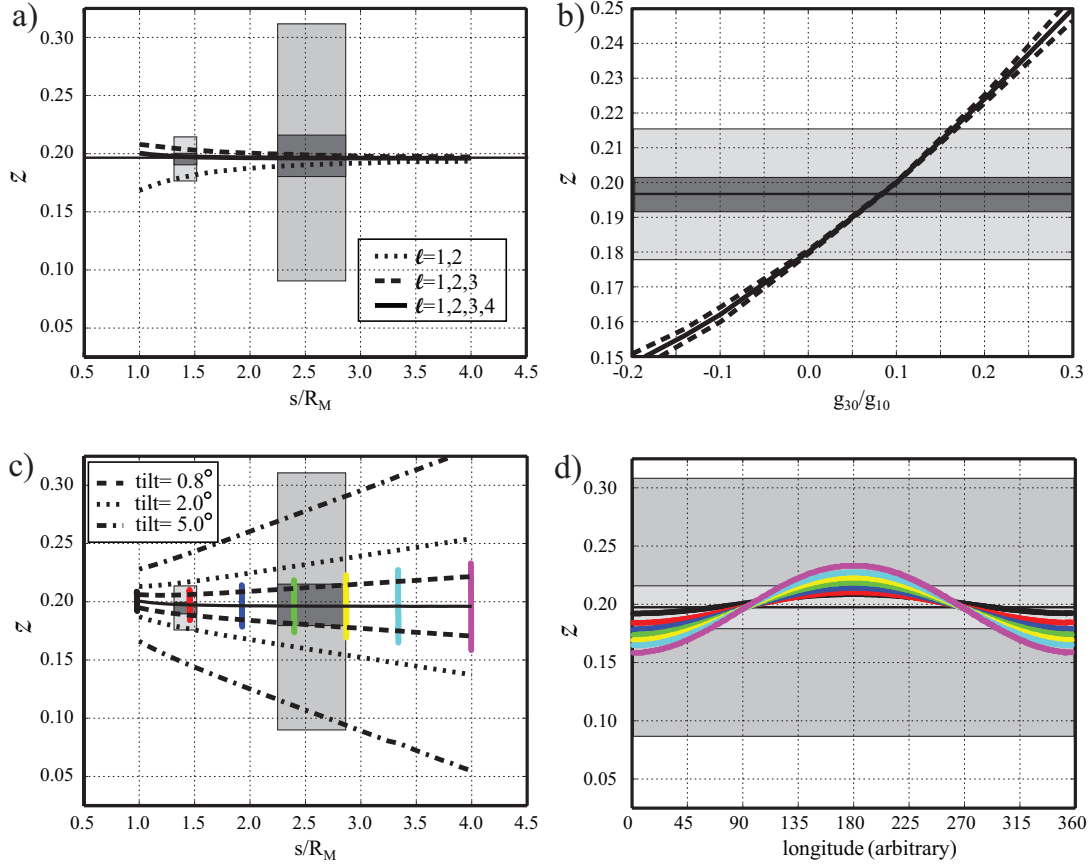


Figure 6: Illustration of the offset dipole model by Anderson et al. [2012]. Panel a) demonstrates how the location of the magnetic equator for the descending (left box) and ascending (right box) orbits is explained by combining axial Gauss coefficients up to degree $\ell = 4$. Light grey boxes illustrate the standard deviation, middle grey boxes the mean three sigma error (see text), and the horizontal black line corresponds to the mean offset. Panel b) illustrates the impact of different relative octupole amplitudes g_{30}/g_{10} . Coloured dots in panels c) and d) show the equator locations found on a dense spherical longitude/latitude grid when an equatorial dipole component g_{11} has been added that corresponds to a dipole tilt of 0.8° . In panel c) the dashed, dotted, and dash-dotted lines show the mean equator offset for each spherical surface of radius s/R_M plus and minus the standard deviation.

ment with different combinations of the spherical harmonic contributions and perform a numerical search for the magnetic equator on a dense longitude/latitude grid for spherical surfaces with radii up to $4R_M$. Panel a) in fig. (6) illustrates how the different axisymmetric contributions in the MODM team up to yield an offset that is nearly independent of the distance to the planet. A large axial quadrupole contribution which amounts to nearly 40% of the axial dipole guarantees a realistic offset for $\rho > 2R_M$. Additional higher harmonic contributions are required to achieve a consistent offset at closer distances. Panel b) in fig. (6) demonstrates that already the relative axial octupole g_{30}/g_{10} is not particularly well constrained and values between 0.05 and 0.12 seem acceptable. Anderson et al. [2012], however, suggest a surprisingly tight range of 0.116 ± 0.009 . Contributions beyond $\ell = 3$ can not be particularly large to retain a nearly constant offset value in the observed range. Constraining them further, however, would require data closer to the planet than presently available. The analysis shows that the mean offset \mathcal{Z} further away from the planet can serve as a proxy for the ratio of the axial quadrupole to axial dipole contribution while the dependence of \mathcal{Z} on the distance closer to the planet provides information on higher order axial contributions.

Anderson et al. [2012] estimate an upper limit for the dipole tilt of $\Theta = 0.8^\circ$. A tilt of the planetary centered dipole causes a longitudinal variation of the magnetic equator location that increases with distance to the planet, as is demonstrated in panels b) and c) of fig. (6). A tilt as large as 2° seems still compatible with the data but the more complex longitudinal dependence of the offset [Anderson et al., 2012] indicates that either higher order harmonics or more likely the solar wind interaction contributes to the variation around the mean offset. A tilt below $< 0.8^\circ$ is also

consistent with a more complete field analysis by Johnson et al. [2012] that includes a parameterized magnetospheric model.

Table 1 compares primary magnetic field characteristics of the MODM with models for other planets and fig. (7) shows the respective radial magnetic surface fields. MODM's large quadrupole contribution is comparable to that inferred for Uranus or Neptune. Unlike the fields of the ice giants, however, Mercury's field is also very axisymmetric, a property it shares with Saturn. The seemingly perfectly axisymmetry of Saturn's field is also the reason for the small spread $\Delta\mathcal{Z}$ of magnetic equator locations for this planet. Saturn's relative quadrupole contribution, however, and thus the relative offset is much smaller than at Mercury.

Magnetic harmonics where the sum of degree ℓ and order m is odd (even) represent equatorially anti-symmetric (symmetric) field contributions. The axial dipole field is thus equatorially anti-symmetric while the axial quadrupole field is symmetric. Mercury's field has a significant equatorially symmetric contribution because of the strong axial quadrupole. Another measure related to the equatorial symmetry breaking is the hemisphericity

$$H = \frac{B_N - B_S}{B_N + B_S} \quad (3)$$

where B_N and B_S are the rms surface field amplitudes in the northern and southern hemispheres, respectively. Due to the offset dipole geometry, the Hermean magnetic field is significantly stronger in the northern than in the southern hemisphere so that the hemisphericity reaches a relatively large value of 0.2. In conclusion, Mercury's magnetic field is not only very weak but also has a peculiar geometry unlike any other planet in our solar system that combines a relatively large axial quadrupole contribution with a very small dipole tilt.

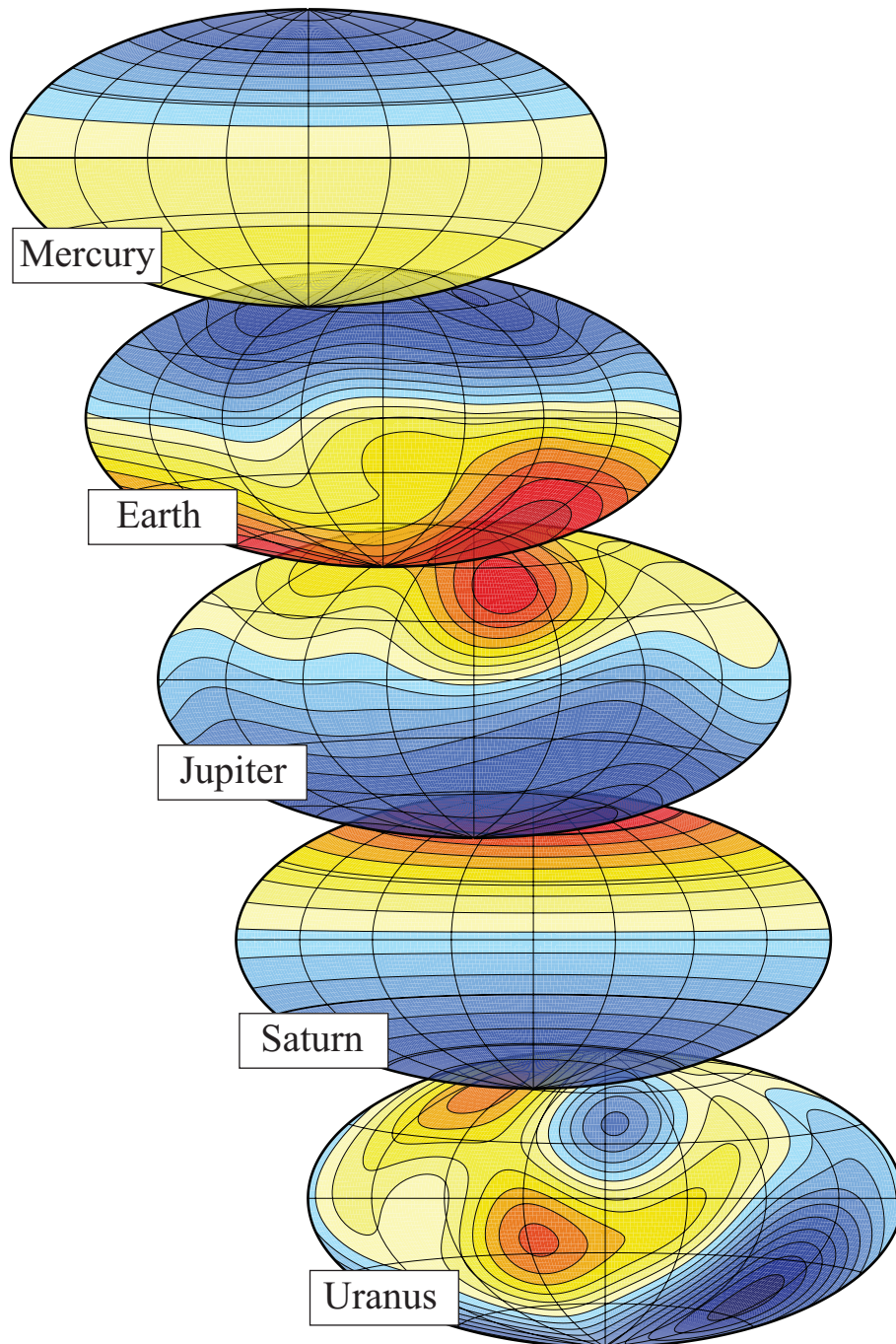


Figure 7: Comparison of different radial magnetic fields at planetary surface. Blue (red and yellow) indicates radially inward (outward) field. See table 1 for information on the different field models.

Quantity	MODM	Earth	Jupiter	Saturn	Uranus
g_{10} [nT]	-190 ± 10	$-29\,560$	$420\,500$	$21\,191$	$11\,855$
tilt [°]	< 0.8	10.2	9.5	< 0.06	58.8
g_{20}/g_{10}	0.392 ± 0.010	0.079	-0.012	0.075	-0.496
g_{30}/g_{10}	0.116 ± 0.009	-0.045	-0.004	0.112	0.353
g_{40}/g_{10}	0.030 ± 0.005	-0.031	-0.040	0.003	0.034
H	0.20	0.017	0.045	0.050	0.251
$\bar{\mathcal{Z}}$	2.0×10^{-1}	2.6×10^{-2}	3.5×10^{-3}	3.8×10^{-2}	5.3×10^{-2}
$\bar{\mathcal{Z}}_d$	2.0×10^{-1}	3.6×10^{-3}	2.8×10^{-2}	4.0×10^{-2}	1.6×10^{-1}
$\Delta\bar{\mathcal{Z}}$	$1.7 \times 10^{-2}(1.1 \times 10^{-1})$	2.2×10^{-1}	1.6×10^{-1}	2.9×10^{-3}	1.0
$\Delta\bar{\mathcal{Z}}_d$	$7.5 \times 10^{-3}(1.9 \times 10^{-2})$	1.3×10^{-1}	9.3×10^{-2}	8.5×10^{-4}	6.6×10^{-1}

Table 1: Comparison of Mercury’s offset dipole model MODM [Anderson et al., 2012] with magnetic field models for other planets: the Grimm model [Lesur et al., 2012] for Earth, the VIP4 model [Connerney et al., 1998] for Jupiter, the model by Cao et al. [2012] for Saturn, and the model by Holme and Bloxham [1996] up to degree $\ell = 4$ for Uranus. The neptunian magnetic field is similar to the field of Uranus and has therefore not been included. The last four lines list mean offset values $\bar{\mathcal{Z}}$ for all spherical surfaces up to $4R$ and the mean offset $\bar{\mathcal{Z}}_d$ for the distances between $1.3R$ and $1.5R$ covered by MESSENGER’s descending orbits. R refers to the planetary radius (1 bar level for gas planets). $\Delta\bar{\mathcal{Z}}$ and $\Delta\bar{\mathcal{Z}}_d$ are the related standard deviations. For Mercury, we list the deviation caused by an 0.8° tilt and also the observed standard deviations in brackets.

The time averaged residual field after subtracting the internal and external field models by Johnson et al. [2012] from the observational data is surprisingly strong with amplitudes of up to 45 nT at 300 km altitude above Mercury’s surface [Purucker et al., 2012]. The fact that the residual field is concentrated at high northern latitudes, is relatively small scale, and correlates with the boundary of the northern volcanic plains to a fair degree points towards crustal remanent magnetization, though an internal field contribution can also not be excluded. A crustal origin would suggest that Mercury’s dynamo is long lived and probably older than 3.5 Gyr. Since the residual field opposes the current dipole direction, the dynamo must have reversed its polarity at least once. This would put valuable constraints on thermal evolution models and dynamo simulations for Mercury.

5 Modelling Mercury’s Internal Dynamo

5.1 Dynamo Theory

Numerical dynamo simulations solve for convection and magnetic field generation in a viscous, electrically conducting, and rotating fluid. Since the solutions are very small disturbances around an adiabatic, well mixed, non-magnetic, and hydrostatic background state, only first order terms are taken into account. For terrestrial planets, the mild density and temperature variations of the background state are typically neglected in the so called Boussinesq approximation [Braginsky and Roberts, 1995]. The mathematical formulation of the dynamo problem is then given by the Navier-

Stokes equation

$$\begin{aligned} \text{E} \frac{d\mathbf{U}}{dt} = & -\nabla P - 2\hat{\mathbf{z}} \times \mathbf{U} + \text{Ra} \frac{r}{r_o} C \hat{\mathbf{r}} \quad (4) \\ & + \frac{1}{\text{Pm}} (\nabla \times \mathbf{B}) \times \mathbf{B} + \text{E} \nabla^2 \mathbf{U} , \end{aligned}$$

the induction or dynamo equation

$$\frac{\partial \mathbf{B}}{\partial t} = (\mathbf{B} \cdot \nabla) \mathbf{U} + \frac{1}{\text{Pm}} \nabla^2 \mathbf{B} , \quad (5)$$

the codensity evolution equation

$$\frac{dC}{dt} = \frac{1}{\text{Pr}} \nabla^2 C + q , \quad (6)$$

the flow continuity equation

$$\nabla \cdot \mathbf{U} = 0 , \quad (7)$$

and the magnetic continuity equation

$$\nabla \cdot \mathbf{B} = 0 . \quad (8)$$

Here, d/dt stands for the substantial time derivative $\partial/\partial t + \mathbf{U} \cdot \nabla$, \mathbf{U} is the convective flow, \mathbf{B} the magnetic field, P is a modified pressure that also contains centrifugal effects, and C is the codensity.

The equations are given in a non-dimensional form that uses the thickness of the fluid shell $d = r_o - r_i$ as a length scale, the viscous diffusion time d^2/ν as a time scale, the codensity difference ΔC across the shell as the codensity scale, and $(\bar{\rho}\mu\lambda\Omega)^{1/2}$ as the magnetic scale. Here, r_i and r_o are the radii of the inner and outer boundary, respectively, ν is the kinematic viscosity, $\bar{\rho}$ the reference state core density, μ the magnetic permeability, λ the magnetic diffusivity, and Ω the rotation rate.

The problem is controlled by five dimensionless parameters: the Ekman number

$$\text{E} = \frac{\nu}{\Omega d^2} , \quad (9)$$

the Rayleigh number

$$\text{Ra} = \frac{\bar{g}_o \alpha \Delta c d^3}{\kappa \nu} \quad (10)$$

the Prandtl number

$$\text{Pr} = \frac{\nu}{\kappa} , \quad (11)$$

the magnetic Prandtl number

$$\text{Pm} = \frac{\nu}{\lambda} , \quad (12)$$

and the aspect ratio

$$a = r_i/r_o . \quad (13)$$

These five dimensionless parameters replace the much larger number of physical properties of which the thermal and/or compositional diffusivity κ , the thermal and/or compositional expansivity α , and the outer boundary reference gravity \bar{g}_o have not been defined so far.

Convection is driven by density variations due to super-adiabatic temperature gradients — only this component contributes to convection — or due to deviations from a homogeneous background composition. Possible sources for thermal convection are secular cooling, latent heat, and radiogenic heating. Possible sources for compositional convection are the light elements released from a growing inner core and iron from an iron snow zone. To simplify computations, both types of density variation are often combined into one variable called codensity C despite the fact that the molecular diffusivities of heat and chemical elements differ by orders of magnitude. The approach is often justified with the argument that the small scale turbulent mixing, which can not be resolved in the numerical simulation, should result in larger effective turbulent diffusivities that are of comparable magnitude [Braginsky and Roberts, 1995]. This has the additional consequence that the ‘turbulent’

Prandtl number and magnetic Prandtl number would become of order one [Braginsky and Roberts, 1995]. The codensity evolution equation (6) contains a volumetric source/sink term q that can serve different purposes depending on the assumed buoyancy sources. For convection driven by light elements released from the inner core, q acts as a sink that compensates the respective source. When modelling secular cooling, the outer boundary is the sink and q the balancing volumetric source [Kutzner and Christensen, 2000]. For iron snow that remelts at depth q should be positive in the snow zone but negative in the convective zone underneath.

Typically, no-slip boundary conditions are assumed for the flow. For the condensity, either fixed codensity or fixed flux boundary conditions are used. The latter translates to a fixed radial gradient and requires a modification of the Rayleigh number (10) where ΔC then stands for the imposed gradient times the length scale d . For terrestrial planets, the much slower evolving mantle controls how much heat is allowed to leave the core, so that a heat flux condition is more appropriate. Lateral variations on the thermal lower mantle structure translate into an inhomogeneous core-mantle boundary heat flux [Aubert et al., 2008]. Since the electrical conductivity of the rocky mantle in terrestrial planets is orders of magnitudes lower than that of the core, the magnetic field can be assumed to match a potential field at the interface $r = r_o$. This matching condition can be formulated as a magnetic boundary condition for the individual spherical harmonic field contributions [Christensen and Wicht, 2007]. A simplified induction equation (5) must be solved for the magnetic field in a conducting inner core which has to match the outer core field at r_i . We refer to Christensen and Wicht [2007] for a more detailed discussion of dynamo theory and the numerical methods employed to solve the sys-

tem of equations.

Explaining the weakness of Mercury’s magnetic field proved a challenge for classical dynamo theory. In convectively driven core dynamos, the Lorentz force and thus the magnetic field needs to be sufficiently strong to influence the flow and thereby saturate magnetic field growth. The impact of the Lorentz force is often expressed via the Elsasser number

$$\Lambda = B^2 / \rho \mu \lambda \Omega \quad (14)$$

where B is the typical magnetic field strength. The Elsasser number estimates the ratio of the Lorentz to the Coriolis force which is known to enter the leading order convective force balance. For Earth, Λ is of order one which suggests that the Lorentz force is indeed significant. For Mercury, however, extrapolating the measured surface field strength to the planet’s core mantle boundary yields $\Lambda_{cmb} \approx 10^{-5}$, a value much too low to be compatible with an Earth-like convectively driven core dynamo [Wicht et al., 2007]. Several authors therefore pursued alternative theories like crustal magnetization or a thermo-electric dynamo (see Wicht et al. [2007] for an overview).

However, convectively driven core dynamos remain the preferred explanation since different modifications of the numerical models originally developed to explain the geodynamo successfully reduced the surface field strength towards more Mercury like values (for recent overviews see Wicht et al. [2007], Stanley and Glatzmaier [2010], Schubert and Soderlund [2011]). We revisit several of these models in the following and test whether they are consistent with MESSENGER magnetic field data.

Model	MODM	E5R6	E5R36	E5R45	CW2	CW3	CW4	Y_{10} BD	Y_{10} ID	Y_{20}
Ra	—	2×10^7	1.2×10^8	1.5×10^8	2×10^8	4×10^8	6×10^8	4×10^7	4×10^7	4×10^7
E	10^{-13}	3×10^{-5}	3×10^{-5}	3×10^{-5}	10^{-4}	10^{-4}	10^{-4}	10^{-4}	10^{-4}	10^{-4}
Pm	10^{-6}	1	1	1	3	3	3	2	2	2
Pr	0.1	1	1	1	1	1	1	1	1	1
a	—	0.35	0.35	0.35	0.50	0.50	0.50	0.35	0.35	0.20
Ro_ℓ	8	0.02	0.10	0.18	0.42	2.7	3.6	0.11	0.06	0.05
Λ_{cmb}	10^{-5}	2.2×10^{-2}	1.8×10^{-1}	1.6×10^{-2}	4.9×10^{-4}	1.9×10^{-4}	4.7×10^{-5}	1.8×10^{-1}	1.9×10^{-1}	4.0×10^{-2}
$ g_{10} $ [nT]	190	8.8×10^3	2.6×10^4	1.4×10^3	1.4×10^3	924	432	2.1×10^4	1.7×10^4	8.3×10^3
tilt [°]	< 0.8	0	2.5	38.1	3.5	4.2	8.6	3.4	10.7	8.2
$ g_{20}/g_{10} $	0.39	0	0.34	3.8	0.08	0.16	0.31	0.06	0.25	0.52
H	0.20	0	0.02	0.11	0.05	0.09	0.09	0.04	0.20	0.23
$ \bar{Z} $	2.0×10^{-1}	0	2.2×10^{-2}	2.1×10^{-1}	4.0×10^{-2}	8.1×10^{-2}	8.4×10^{-2}	3.8×10^{-2}	1.5×10^{-1}	2.0×10^{-1}
$\Delta \bar{Z}$	1.7×10^{-2} (1.1×10^{-1})	0	6.9×10^{-2}	8.6×10^{-1}	8.3×10^{-2}	2.4×10^{-1}	1.1×10^{-1}	2.2×10^{-1}	2.3×10^{-1}	

Table 2: Comparison of Mercury’s dynamo parameter and properties with nine dynamo models that have been (re)analysed here. For Mercury we list the MODM while time averaged local Rossby numbers Ro_ℓ and magnetic field properties are listed for the numerical simulations. Mercury’s core Rayleigh number and aspect ratio are basically unconstrained but and we have assumed an Earth-like value of $a = 0.35$ to calculate the Ekman number. Other Mercury parameters follow Schubert and Soderlund [2011] and Olson and Christensen [2006]. Two models with a Y_{10} CMB heat flux pattern are listed, one is bottom driven (BD) while the other is internally driven (ID). The model with a Y_{20} pattern is internally driven.

All dynamo simulations have the problem that numerical limitations prevent the use realistic diffusivities. For example, the viscous diffusivity is many orders of magnitude too large to damp the very small scale convection motions that cannot be resolved with the available computer power. Dynamo modelers typically fix the Ekman number E , the ratio of viscous to Coriolis forces, to the smallest value accessible with the numerical resources. The most advanced computer simulations reach down to $E = 10^{-7}$ which is still many orders of magnitude larger than the planetary value of $E \approx 10^{-12}$ (see table 2). The Prandtl number Pr can assume realistic values but the magnetic Prandtl number Pm has to be set to a value that guarantees dynamo action. Because of the increased viscous diffusivity, Pm is also orders of magnitudes too large. The Rayleigh number is then adjusted to a value that yields the desired dynamics. The fact that numerical Dynamo simulations are very successful in reproducing many aspects of planetary dynamos suggest that at least the large scale dynamics responsible for producing the observable magnetic field is captured correctly.

The simulation results must be rescaled to the planetary situation. For simplicity, we will rescale the magnetic field strength by assuming that the Elsasser number would not change when pushing the parameter towards realistic values. Assuming Mercury’s rotation rate, mean core density, magnetic permeability and magnetic diffusivity then allows the deduce the dimensional magnetic field strength via eqn. (14). Note, however, that other scalings have been proposed [Christensen, 2010] and may lead to somewhat different answers.

5.2 Standard Earth-like Dynamo Models

To highlight the difficulties of classical dynamo simulations to reproduce the Hermean mag-

netic field, we start with analysing three models that have been explored in the geomagnetic context by Wicht et al. [2011b]. All have the same Ekman ($E = 3 \times 10^{-5}$), Prandtl number ($Pr = 1$), magnetic Prandtl number ($Pm = 1$), aspect ratio ($a = 0.35$), use rigid and fixed co-density boundary conditions and are driven by a growing inner core. They differ only in the Rayleigh number: Model E5R6 has the lowest Rayleigh number of $Ra = 2 \times 10^7$, six times the critical value for onset of convection. Model E5R36 has an intermediate Rayleigh number of $Ra = 1.2 \times 10^8$ while model E5R45 has the largest Rayleigh number at $Ra = 1.5 \times 10^8$. All model parameters are listed in table 2.

Fig. (8) shows the time evolution of the axial dipole strength, the dipole tilt, the mean magnetic equator offset \bar{Z} for up to four planetary radii (assuming Mercury’s thin crust), and the related standard deviation $\Delta\bar{Z}$. At the lowest Rayleigh number, convective driving is too small to break the equatorial symmetry. The magnetic field is therefore perfectly equatorially anti-symmetric and very much dominated by the axial dipole contribution. Dipole tilt, offset and standard deviation therefore vanish. At the intermediate Rayleigh number the solution is sufficiently dynamic and asymmetric to be considered very Earth-like [Wicht et al., 2011b, Christensen et al., 2010]. While the axial quadrupole and other equatorially symmetric field contributions have grown, the strong axial dipole still clearly dominates. The mean offset \bar{Z} therefore remains small but oscillates around zero since neither the northern nor the southern hemisphere are preferred in the dynamo setup. The spread $\Delta\bar{Z}$ is of the same order as the offset itself mainly because of the Earth-like dipole tilt. The inertial contributions in the flow force balance have increased to a point where magnetic field reversals can be expected [Christensen and Aubert, 2006, Wicht et al., 2011b].

Christensen and Aubert [2006] introduced

the local Rossby number

$$\text{Ro}_\ell = \frac{U}{L\Omega} \quad (15)$$

to quantify the ratio of inertial to Coriolis forces. Here, U is the rms flow amplitude and L is a typical flow length scale defined by

$$L = d\pi \frac{\sum U_\ell}{\sum \ell U_\ell} . \quad (16)$$

U_ℓ is the rms flow amplitude of spherical harmonic contributions with degree ℓ . The Coriolis force is responsible for organizing the flow into quasi two-dimensional convective columns which tend to produce the larger scale dipole dominated magnetic field. Inertia and in particular the non-linear advective term, on the other hand, is responsible for the mixing of different scales and therefore the braking of flow symmetries. At $\text{Ro}_\ell = 0.10$ inertia is likely large enough in model E5R36 to trigger reversals though no such event has been observed in the relatively short period we could afford to simulate.

Christensen and Aubert [2006] report that this typically happens for $\text{Ro}_\ell \approx 0.1$, a limit clearly exceeded at $\text{Ro}_\ell = 0.18$ in model E5R45. Smaller scale contributions dominate the now multipolar magnetic field which also becomes very variable in time and constantly changes its polarity [Wicht et al., 2011b]. Consequently, the offset also varies rapidly and may even exceed Mercury’s offset value at times where the axial dipole is particularly low (see fig. (8)b). While axial dipole and offset can assume Mercury-like values during brief periods in time, this is not true for the dipole tilt and $\Delta\bar{Z}$. The larger Rayleigh number promotes not only the axial quadrupole but higher harmonics and non-axial field contribution in general. The tilt is therefore typically rather large and the magnetic equator covers a wide latitude range. Closer to the planet, even two

or more closed lines with $B_\rho = 0$ can be found at a given radius.

Olson and Christensen [2006] estimate a large local Rossby number of $\text{Ro}_\ell \approx 8$ for Mercury, mainly because of the planet’s slow rotation rate. This suggests that the dynamo produces a multipolar field at least as complex as in the large Rayleigh number model E5R45. This is at odds with the observations unless we could add a physical mechanism to the model that would filter out smaller scale field contributions while retaining the strong axial quadrupole. As we discuss in the following, the stably stratified layer underneath Mercury’s core-mantle boundary (See section 2) may meet these requirements.

5.3 Dynamos with a stably stratified outer layer

The idea of a stably stratified layer in the outer part of a dynamo region was first proposed by Stevenson [1980] to explain Saturn’s very axisymmetric magnetic field. The immiscibility of Helium and Hydrogen in Saturn’s metallic envelope [Lorenzen et al., 2009] may cause Helium to precipitate into the deeper interior. Similar to the iron snow scenario discussed in section 2 this process may establish a stabilizing Helium gradient in the rain zone.

Christensen [2006] and Christensen and Wicht [2008] adopt this idea for Mercury. They propose that the subadiabatic heat flux through the CMB leads to the stable stratification but since they use a condensity approach the model is not able to distinguish between thermal and compositional effects. The magnetic field that is produced in the convecting deeper core region has to diffuse through the largely stable outer layer so that the magnetic skin effect applies here. The time variability of the magnetic field increases with spatial complexity [Christensen and Tilgner, 2004, Lhuillier et al., 2011]. The higher harmonic

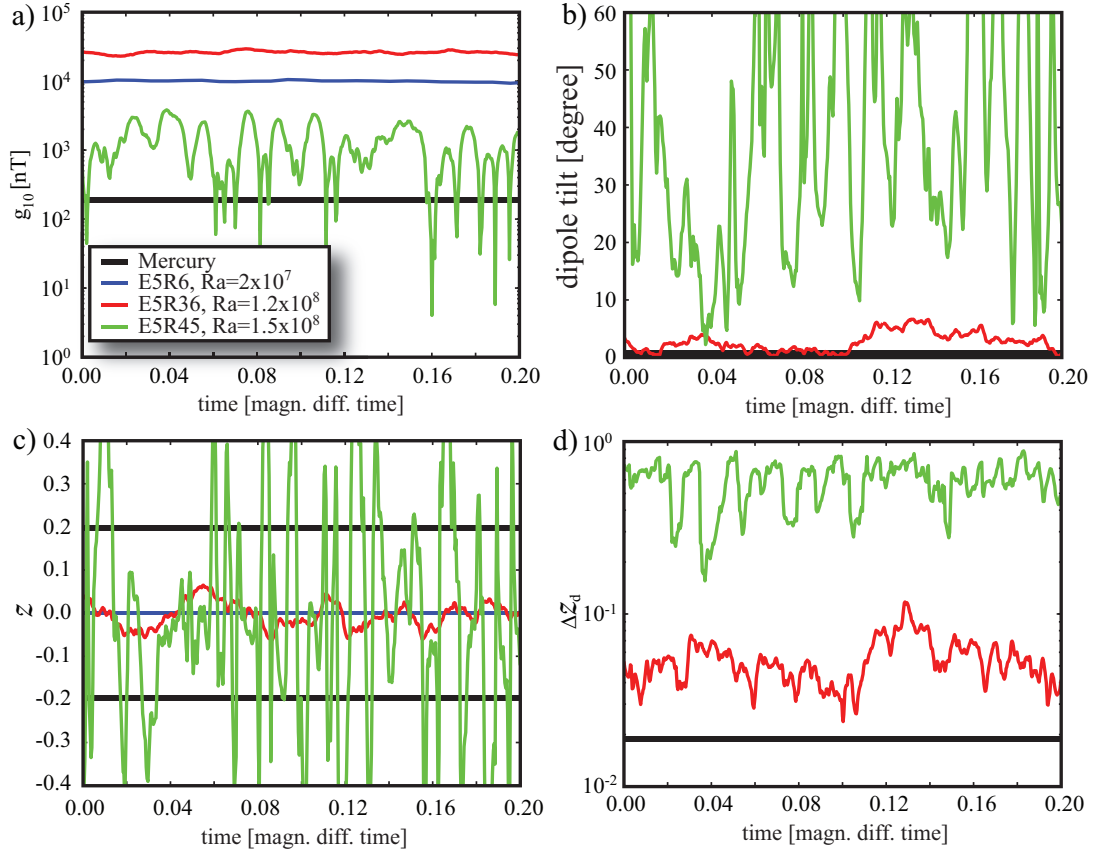


Figure 8: Time evolution of three standard dynamo models with different Rayleigh numbers. The thick black horizontal lines indicate the MESSENGER offset dipole model. Panel a) shows the axial dipole coefficient, panel b) the dipole tilt, panel c) the mean offset Z averaged over all radii up to $4R_M$, and panel d) shows the standard deviation for the offset in the distance range of the descending orbits ΔZ_d . For the numerical simulations time is given in units of the magnetic diffusion time $\tau_\lambda = d^2/\lambda$. When assuming an Earth-like aspect ratio of 0.35 and a magnetic diffusivity of $\lambda = 1$ the Hermean magnetic diffusion time amounts to $\tau_\lambda \approx 54$ kyr.

field contributions are therefore more significantly damped by the skin effect than for example dipole or quadrupole. Zonal motions that may still penetrate the stable layer cannot lead to significant dynamo action but further increase the skin effect for non-axisymmetric field contributions. Thanks to this filtering effect, the multipolar field of a high Ro_ℓ dynamo should look more Mercury-like when reaching the planetary surface.

Testing different dynamo setups, Christensen [2006] and Christensen and Wicht [2008] demonstrate that the surface field is indeed weaker and less complex when a sizable stable layer is included. We reanalyse the models 2,3, and 4 published in Christensen and Wicht [2008] to test whether they are consistent with the new MESSENGER data. All three models, that we will refer to as CW2, CW3, and CW4 in the following, have a solid inner core that occupies the inner 50% in radius and a stable region that occupies the outer 28%. Thus only a relatively thin region is left to host the active dynamo. Like for the standard models explore above, all three cases have the same Ekman number ($E = 10^{-4}$), Prandtl number ($Pr = 1$), and magnetic Prandtl number ($Pm = 3$) but differ in Rayleigh number. Once more, they use rigid flow boundary conditions and are driven by a growing inner core. The model parameters are listed in table 2.

Fig. (9) shows the time evolution of the axial dipole contribution, the dipole tilt, the mean offset \bar{Z} , and of its standard deviation $\Delta\bar{Z}$. At the lowest Rayleigh number of $Ra = 2 \times 10^8$ in CW2, the magnetic field strength is already significantly weaker and the dipole tilt and offset standard deviation can actually reach Mercury-like small values. The axial dipole component, however, is still somewhat strong and dominant and the offset value therefore too small. Increasing the Rayleigh number to $Ra = 4 \times 10^8$ in model CW3 decreases the axial dipole in absolute and rela-

tive terms. The mean tilt, offset, and spread increase, but there are times when Mercury-like field geometries are approached. The axial dipole is still by a factor four too strong. At $Ra = 4 \times 10^8$ in model CW4, however, the axial dipole can even become smaller than at Mercury. The field is very time dependent during these episodes and is characterized by large dipole tilts and $\Delta\bar{Z}$ values since higher harmonic and non-axisymmetric field contributions dominate. Very Mercury-like fields, that combine small dipole tilts with larger offset values but small offset standard deviations, can be found during brief periods when the axial dipole is somewhat stronger than the Mercury value.

Fig. (10) illustrates the location of the magnetic equator for two particularly Mercury-like snapshots in the two larger Rayleigh number models CW3 and CW4. Fig. (11) directly compares the respective radial magnetic fields with the MESSENGER model. Both figures demonstrate that solutions very similar to the offset dipole field proposed for Mercury can be found with a stably stratified outer core layer and a sufficiently high Rayleigh number. However, the magnetic field varies considerably in time and since neither hemisphere is preferred the offset can switch from north to south and back. The particular offset dipole configuration encountered by MESSENGER would thus only be transient and representative for only a few percent of the time at best.

Fig. (12) compares the time averaged spherical harmonics surface spectrum of models CW3 and CW4 with MODM, confirming that the relative quadrupole contribution and thus the equator offset is typically too low. The relative energy in spherical harmonic degrees $\ell = 3$ and 4, however, agrees quite well with MESSENGER observations.

Manglik et al. [2010] explore what happens to the stable layer when giving up the codensity formulation. They use a so-called double-

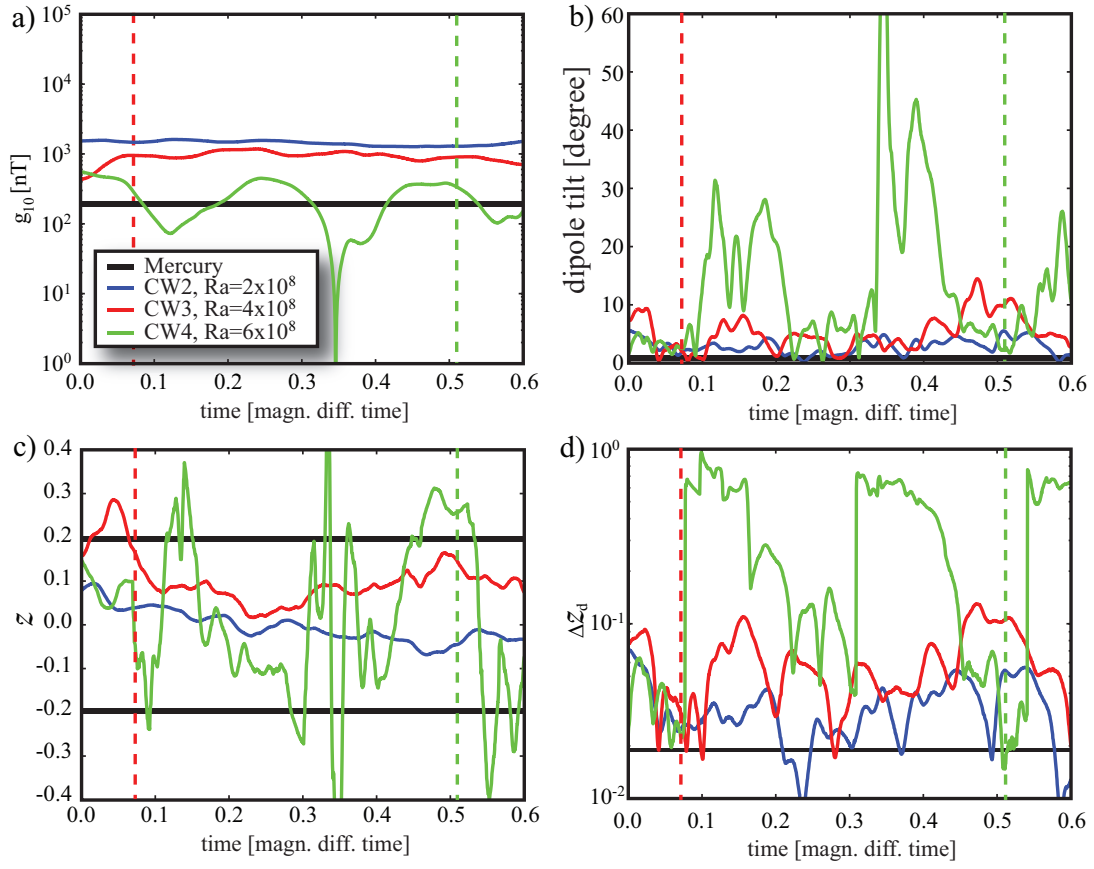


Figure 9: Time evolution of three dynamo models with a stably stratified layer. See fig. (8) for more explanation. The dashed vertical red and green lines mark the times for the snapshots illustrated in fig. (10) and fig. (11).

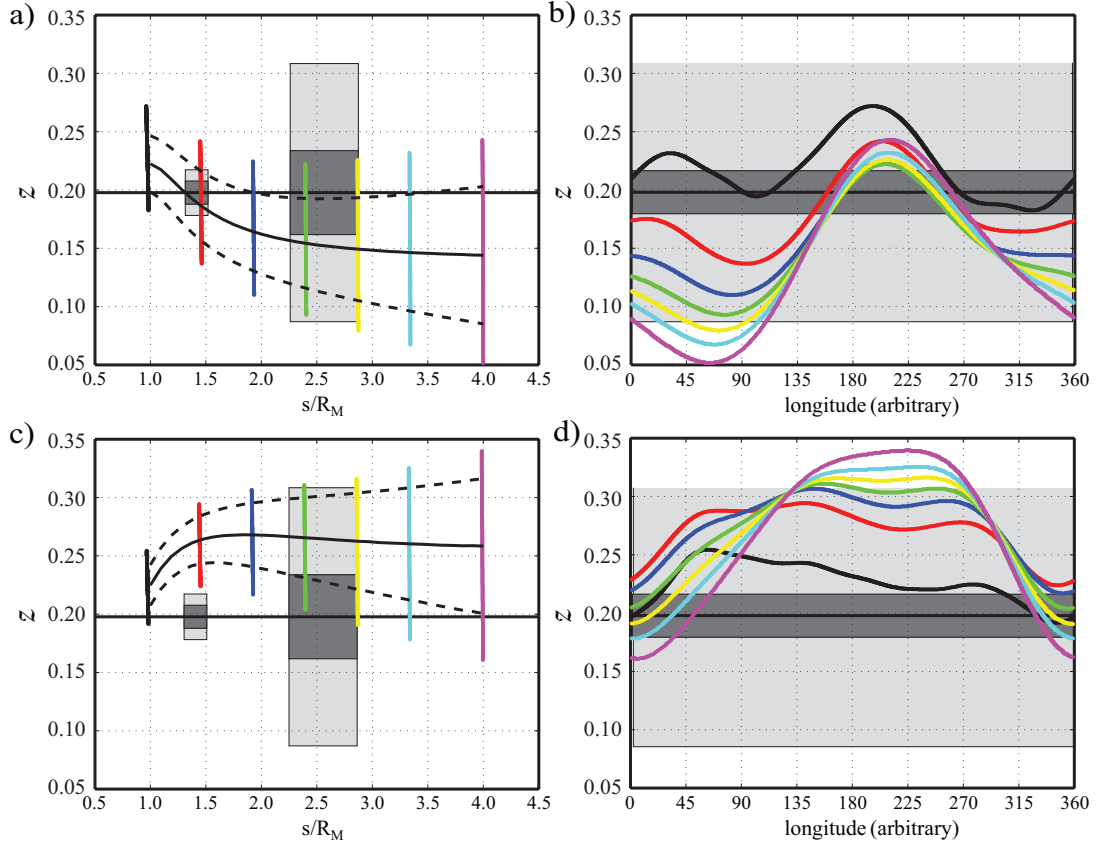


Figure 10: Magnetic equator location for two snapshots in dynamo models CW3 (top panels) and CW4 (bottom panels). The respective snapshot times have been marked by the vertical dashed lines in fig. (9). Coloured dots show the equator locations found on a dense spherical longitude/latitude grid. The curved solid lines in panels a) and b) show the mean equator offset for each spherical surface with radius s/R_M , the dashed lines show the mean offset plus and minus the standard deviation. Thick horizontal lines illustrate the mean offset measured by the MESSENGER magnetometer while mid gray and light grey boxed show mean three sigma error and standard deviation for descending (left) and ascending orbits (right), respectively.

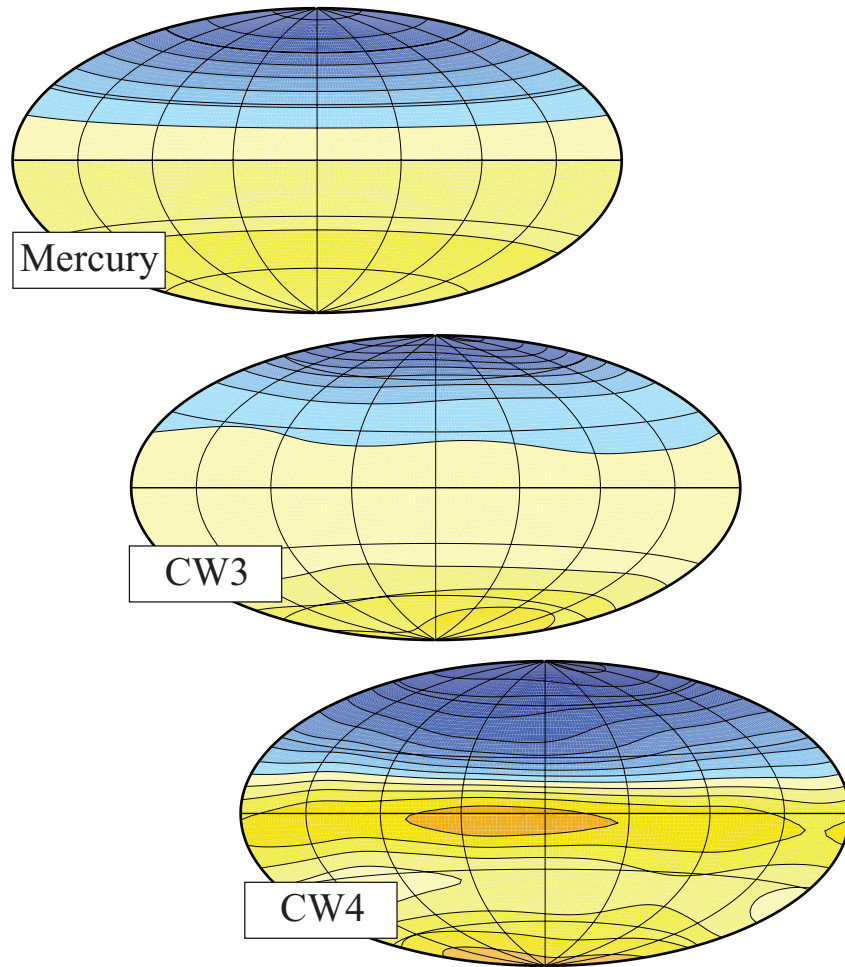


Figure 11: Comparison of the MODM radial magnetic field for Mercury with the two particularly Mercury-like snapshots in models CW3 and CW4 already depicted in fig. (10). Blue (red and yellow) indicates radially inward (outward) field.

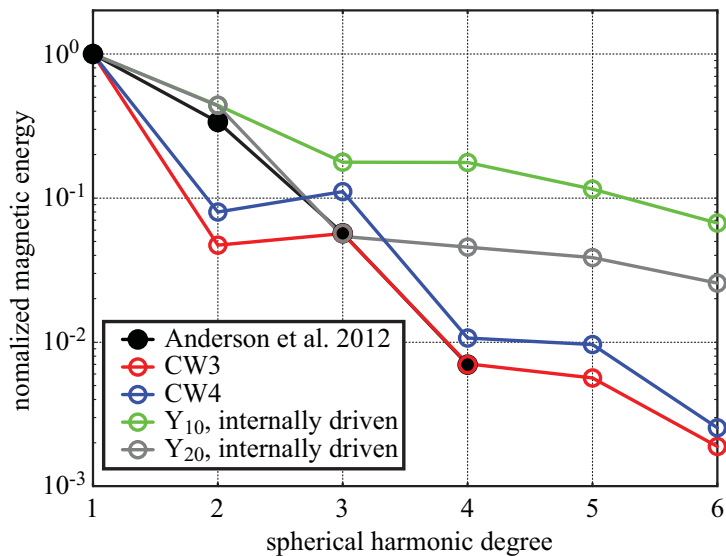


Figure 12: Comparison of the normalized MODM surface spectrum by Anderson et al. [2012] with time averaged spectra for four different dynamo models: the dynamo models CW3 and CW4 that incorporate a stably stratified outer layer [Christensen and Wicht, 2008] and models with an inhomogeneous core-mantle boundary heat flux following a spherical harmonic Y_{10} or Y_{20} pattern, respectively.

diffusive approach where two equations of the form of eqn. (6) separately describe the evolution of temperature and composition. When assuming a compositional diffusivity that is one order of magnitude lower than the thermal diffusivity, the compositional plumes that rise from the inner core boundary already stay significantly narrower than their thermal counterparts. This allows them to more easily penetrate and destroy the stable outer layer. The desirable filtering effect is greatly lost unless the sulphur concentration is below 1 wt% where compositional convection starts to play an inferior role. For such a low light element concentration, however, Mercury’s core would likely be completely solid today.

The iron snow mechanism discussed in section 2 offers an alternative scenario where the stable stratified layer is likely to persist even in a double-diffusive approach. The sulfur gradient that develops in the iron snow zone is po-

tentially much more stabilizing than the sub-adiabatic thermal gradient assumed by Christensen and Wicht [2008] and Manglik et al. [2010]. Furthermore, the additional convective driving source represented by the remelting snow would counteract the effects of the more sulfur rich plumes rising from a growing inner core.

5.4 Inhomogeneous boundary conditions

As already discussed in section 1, an inhomogeneous heat flux through the CMB is an obvious way to break the north/south symmetry and enforce a more permanent offset of the magnetic equator. To explain the stronger magnetization of the southern crust on Mars several authors explored a variation following a spherical harmonic function Y_{10} of degree $\ell = 1$ and order $m = 0$ [Stanley et al., 2008, Amit et al.,

2011, Dietrich and Wicht, 2013]. The total CMB heat flux is then given by

$$q = q_0 (1 - q_{10}^* \cos \theta) \quad (17)$$

where q_0 is the mean heat flux, q_{10}^* the relative amplitude of the lateral variation, and θ the colatitude. Positive values of q_{10}^* are required at Mars and negative values should enforce the stronger northern magnetic field observed on Mercury.

To explore the impact of the CMB heat flux pattern we use dynamo simulations in the parameter range discussed by Dietrich and Wicht [2013] and Cao et al. [2014]. The parameters are $E = 10^{-4}$, $Ra = 4 \times 10^7$, $Pr = 1$, $Pm = 2$, and $a = 0.35$. Once more, rigid boundary conditions are used and we impose the heat flux at the outer boundary. The Rayleigh number is then defined based on the mean CMB heat flux [Dietrich and Wicht, 2013]. Fig. (13) demonstrates that a relative variation amplitude of $q_{10} = -0.10$ is nearly sufficient to enforce the observed offset when the dynamo is driven by homogeneously distributed internal sources. These may either model secular cooling, radioactive heating, or the remelting of iron snow. We have used a codensity formulation here and set the codensity flux from the inner core boundary to zero. Significantly larger heat flux variations are required for the other end member when the dynamo is driven by bottom sources that mimic a growing inner core. This is consistent with the findings by [Hori et al., 2012] who report that the impact of thermal CMB boundary conditions is generally larger for internally driven than bottom driven simulations.

Another not so obvious method to promote a north/south asymmetry is to increase the heat flux through the equatorial region. Cao et al. [2014] explore a Y_{20} pattern, which means that the total CMB flux is given by

$$q = q_0 \left(1 - q_{20}^* \frac{1}{2} (3 \cos \theta - 1) \right) . \quad (18)$$

The green line in fig. (13) illustrates that a variation amplitude of $q_{20}^* = 1/3$ causes a more or less persistent Mercury-like offset value. This translates into an increase of the equatorial flux by 17% and a decrease to polar flux by 33%. Cases with an increased heat flux at the poles, i.e. negative values of q_{20}^* , did not yield the desired result. Except for the CMB heat flux pattern and a smaller inner core that only occupies 20% of the radius, the models are identical to the Y_{10} cases explored above. Though the Y_{20} pattern is equatorially symmetric, it promotes an equatorially asymmetric flow and therefore an asymmetric magnetic field production. A preliminary analysis of the system suggest that the Y_{20} pattern significantly decreases the critical Rayleigh number for the onset of equatorially anti-symmetric convection modes, which is very large when the CMB heat flux is homogenous [Landeau and Aubert, 2011].

The inhomogenous CMB heat flux mainly helps to promote a Mercury-like mean offset of the magnetic equator while other important field characteristics seem not consistent with the observations. The field is generally much too strong and the often large dipole tilt and offset spread $\Delta \bar{Z}$ testify that higher harmonic and non-axisymmetric field contributions remain too significant. This is confirmed by the time averaged spectra shown in fig. (12). Adding a stably stratified outer layer, probably in combination with a larger Rayleigh number to bring down the too strong axial dipole contribution, seems like an obvious solution to this problem. This was confirmed by the first results presented by Tian et al. [2013] who explore the combination of the stable layer with the Y_{10} heat flux pattern.

5.5 Alternatives

Several authors varied the inner core size to explore its impact on the dynamo process. Heim-

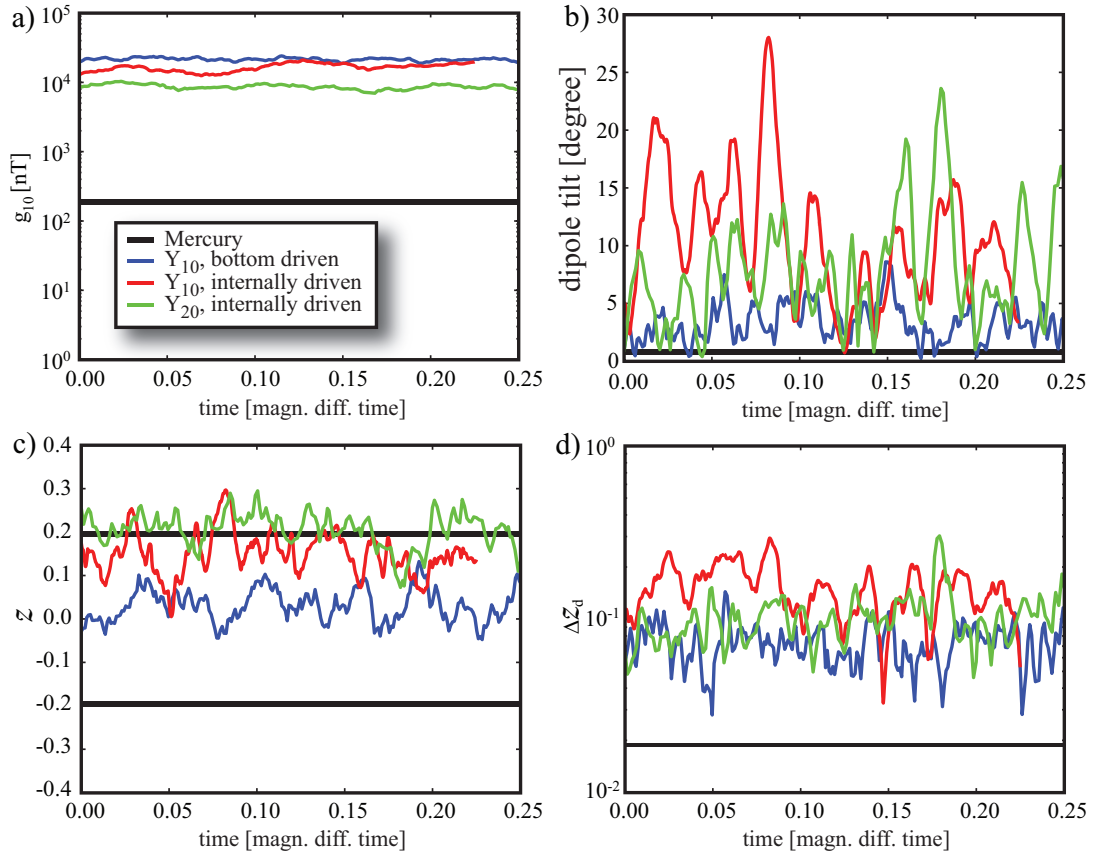


Figure 13: Time evolution of three dynamo models with inhomogeneous core-mantle boundary heat flux. A Y_{10} pattern with increased heat flux through the northern hemisphere but also a Y_{20} pattern with a larger heat flux in the equatorial region promotes a Mercury-like offset. See text and fig. (8) for more explanation.

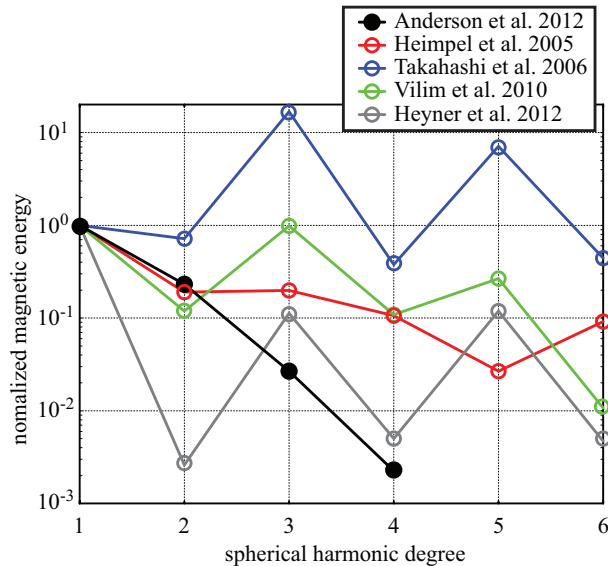


Figure 14: Comparison of the normalized MODM surface spectrum by Anderson et al. [2012] with spectra for different dynamo models. A time averaged spectrum is shown for the models by Vilim et al. [2010] and Heyner et al. [2011a] while the spectra for Heimpel et al. [2005], Takahashi and Matsushima [2006] represent snapshots.

pel et al. [2005] analyse models with aspect ratios between $a = 0.65$ and $a = 0.15$ that are all driven by a growing inner core. They report that the smallest inner core yields a particularly weak magnetic field with a CMB Elsasser number of $\Lambda_{cmb} = 10^{-2}$ when the Rayleigh number is close to onset for dynamo action. This is still more than two orders of magnitude too large for Mercury. Convection and dynamo action are mainly concentrated at only one convective column attached to the inner core. Such localized magnetic field production is not very conducive to maintaining a large scale magnetic field which is confirmed by the magnetic surface spectrum of a model snapshot shown in fig. (14). The relative quadrupole contribution nearly matches the MODM value but the higher harmonic contributions can reach a similar level and are thus too strong. This is also true for the dipole tilt which has a mean value of 8° for this model.

Takahashi and Matsushima [2006] find that the magnetic field strength is also reduced when using a large inner core with $a = 0.7$ in combination with a large Rayleigh number. Once more, the field is still too strong for Mercury with an Elsasser number around $\Lambda_{cmb} = 10^{-2}$ and is also much too small in scale with $\ell = 3$ and 5 contributions dominating the spectrum (see fig. (14)). Stanley et al. [2005] explore even larger inner cores with aspect ratios up to $a = 0.9$ and report particularly weak fields at rather low Rayleigh numbers. The use of stress-free flow boundary conditions set this dynamo model apart from all the other cases discussed here. Field strength, dipole tilt, and offset are highly variable but seem to assume Mercury-like values at times. Little more is published about the field geometry and it seems worth to explore these models further.

Vilim et al. [2010] explore the double snow zone regime that may develop when the sulfur

content in Mercury’s core exceeds 10 wt%, as briefly discussed in section 4. They consider a thin outer snow zone and a thicker zone in the middle of the liquid core in addition to a growing inner core. Since both snow zones are stably stratified the dynamo action is concentrated in the two remaining shells. The magnetic fields that are produced in these two dynamo regions tend to oppose each other which leads to a reduced overall field strength that matches the MESSENGER observation. However, the octupole component is generally too strong while the quadrupole contribution is too weak, as is demonstrated in fig. (14).

Since internal and external magnetic field can reach similar magnitudes at Mercury the latter may actually play a role in the core dynamo. The idea of a feedback between internal and external dynamo processes was first proposed by Glassmeier et al. [2007] for Mercury and further developed in a series of papers [Heyner et al., 2010, 2011a,b]. Because the internal dynamo process operates on time scales of decades to centuries, only the long time-averaged magnetospheric field needs to be considered. This can be approximated by an external axial dipole that opposes the direction of the internal axial dipole within the core. The ratio of the external to internal dipole field depends on the distance of the magnetopause to the planet and thus on the intensity of the internal field. Heyner et al. [2011a] find that the feedback quenches the dynamo field to Mercury-like intensities when the simulation is started off with an already weak field and the Rayleigh number is not too high. These conditions can, for example, be met when dynamo action is initiated with the beginning of iron snow or inner core growth at a period in the planetary evolution where mantle convection is already sluggish and the CMB heat flux therefore low. The feedback process modifies the dipole dominated field by concentrating the flux at higher latitudes. The result is a spec-

trum where the relative quadrupole (and other equatorially anti-symmetric contributions) is too weak while the octupole (and other equatorially symmetric contributions) is too strong (see fig. (14)).

6 Conclusion

The MESSENGER data have shown that Mercury has an exceptional magnetic field [Anderson et al., 2012, Johnson et al., 2012]. The internal field is very weak and has a simple but surprising geometry that is consistent with an axial dipole offset by 20% of the planetary radius to the North. This implies a very strong axial quadrupole but at the same time also small higher harmonic and non-axial contributions, a unique combination in our solar system.

Numerical dynamo models have a hard time to explain these observations. Strong axial quadrupole contributions and thus a significant mean offset of the magnetic equator can be promoted by different measures. Very small and very large inner cores or strong inertial forces are three possibilities that lead to a sizable but also very time dependent axial quadrupole contribution.

A more persistent Mercury-like mean offset can be enforced by imposing lateral variations in the core-mantle boundary heat flux. Pattern with either an increased heat flux in the northern hemisphere or in the equatorial region yield the desired result. They are particularly effective when the dynamo is not driven by a growing inner core but by homogeneously distributed buoyancy sources [Cao et al., 2014]. New models for Mercury’s interior, however, suggest that neither pattern is likely to persist today.

Unfortunately, the measures that promote a stronger axial quadrupole also tend to promote non-dipolar and non-axisymmetric field con-

tributions in general. The offset of the magnetic equator therefore strongly depends on longitude and distance to the planet, which is at odds with the MESSENGER observations. Dynamo simulations by Christensen [2006] and Christensen and Wicht [2008] have shown that a stably stratified outer core layer helps to solve this problem. The magnetic field that is produced in the deeper core regions has to diffuse through this largely passive layer to reach the planetary surface. And since the magnetic field varies in time it is damped by the magnetic skin effect during this process. Higher harmonic and non-axisymmetric contributions are damped more effectively than axial dipole or quadrupole because the variation time scale decreases with increasing spatial complexity. When reaching the surface, the field is therefore not only more Mercury-like in geometry but also similarly weak.

Recent interior models for Mercury suggest that a stable outer core layer may indeed exist. Because of the low pressures in Mercury's outer core, an outer iron snow zone should develop underneath the CMB for mean core sulfur concentration beyond about 2 wt%. As the planet cools, the snow zone extends deeper into the core and a stably stratifying sulfur gradient develops. Since the mean heat flux out of the Hermean core is likely subadiabatic today, thermal effects would further contribute to stabilizing the outer core region. Such a layer is also likely to persist when double-diffusive effects are taken into account [Manglik et al., 2010]. Additional work on the FeS melting behaviour, on Mercury's interior properties, and the planet's thermal evolution is required to better understand and establish this scenario. The possible presence of Si in the Hermean core could further complicate matters [Malavergne et al., 2010].

Dynamo simulations that more realistically model the iron snow stratification and the convective driving in the presence of an iron snow

zone and possibly also a growing inner core seem a logical next step. Lateral variations in the core-mantle boundary heat flux and a feedback with the magnetospheric field are two other features that may play an important role in Mercury's dynamo process.

The Hermean magnetospheric field remains a challenging puzzle despite the wealth of data delivered by the MESSENGER magnetometer. Its small size and high variability complicates the separation of internal and external field contributions, of temporal and spatial variations, and of solar wind dynamics and Mercury's genuine field dynamics. The Bepi-Colombo mission, scheduled for launch in 2016, will significantly improve the situation since two spacecrafts will orbit the planet at the same time, a planetary orbiter build by ESA and a magnetospheric orbiter build by JAXA.

Acknowledgement

Johannes Wicht was supported by the Helmholtz Alliance "Planetary Evolution and Live" and by the Special Priority Programm 1488 "Planetary Magnetism" of the German Science Foundation. D. Heyner was supported by the German Ministerium für Wirtschaft und Technologie and the German Zentrum für Luft- und Raumfahrt under contract 50 QW 1101. We thank Attilio Rivoldini, Tina Rückriehmen, Wieland Dietrich, Hao Cao, Brian Anderson, Karl-Heinz Glassmeier, and Ulrich R. Christensen for helpful discussions. Attilio Rivoldini also kindly provided figure 1.

References

- S. C. Solomon. Some aspects of core formation in Mercury. *Icarus*, 28:509–521, August 1976. doi: 10.1016/0019-1035(76)90124-X.
- N. F. Ness, K. W. Behannon, R. P. Lepping,

- Y. C. Whang, and K. H. Schatten. Magnetic Field Observations near Mercury: Preliminary Results from Mariner 10. *Science*, 185:151–160, July 1974. doi: 10.1126/science.185.4146.151.
- J. A. Slavin, S. M. Krimigis, M. H. Acuña, B. J. Anderson, D. N. Baker, P. L. Koehn, H. Korth, S. Livi, B. H. Mauk, S. C. Solomon, and T. H. Zurbuchen. MESSENGER: Exploring Mercury’s Magnetosphere. *Space Sci. Rev.*, 131:133–160, August 2007. doi: 10.1007/s11214-007-9154-x.
- S. C. Solomon, R. L. McNutt, R. E. Gold, and D. L. Domingue. MESSENGER Mission Overview. *Space Sci. Rev.*, 131:3–39, August 2007. doi: 10.1007/s11214-007-9247-6.
- Brian J Anderson, Catherine L Johnson, Haje Korth, Reka M Winslow, Joseph E Borovsky, Michael E Purucker, James A Slavin, Sean C Solomon, Maria T Zuber, and Ralph L McNutt. Low-degree structure in Mercury’s planetary magnetic field. *Journal of Geophysical Research: Planets (1991–2012)*, 117(E12), 2012.
- C. L. Johnson, M. E. Purucker, H. Korth, B. J. Anderson, R. M. Winslow, M. M. H. Al Asad, J. A. Slavin, I. I. Alexeev, R. J. Phillips, M. T. Zuber, and S. C. Solomon. MESSENGER observations of Mercury’s magnetic field structure. *Journal of Geophysical Research (Planets)*, 117:E00L14, December 2012. doi: 10.1029/2012JE004217.
- N. Olsen, K.-H. Glassmeier, and X. Jia. Separation of the Magnetic Field into External and Internal Parts. *Space Sci. Rev.*, 152: 135–157, May 2010. doi: 10.1007/s11214-009-9563-0.
- B. J. Anderson, C. L. Johnson, H. Korth, M. E. Purucker, R. M. Winslow, J. A. Slavin, S. C. Solomon, R. L. McNutt, J. M. Raines, and T. H. Zurbuchen. The Global Magnetic Field of Mercury from MESSENGER Orbital Observations. *Science*, 333:1859–, September 2011. doi: 10.1126/science.1211001.
- D. E. Smith, M. T. Zuber, R. J. Phillips, S. C. Solomon, S. A. Hauck, F. G. Lemoine, E. Mazarico, G. A. Neumann, S. J. Peale, J.-L. Margot, C. L. Johnson, M. H. Torrence, M. E. Perry, D. D. Rowlands, S. Goossens, J. W. Head, and A. H. Taylor. Gravity Field and Internal Structure of Mercury from MESSENGER. *Science*, 336:214–, April 2012. doi: 10.1126/science.1218809.
- J.-L. Margot, S. J. Peale, S. C. Solomon, S. A. Hauck, II, F. D. Ghigo, R. F. Jurgens, M. Yseboodt, J. D. Giorgini, S. Padovan, and D. B. Campbell. Mercury’s moment of inertia from spin and gravity data. *Journal of Geophysical Research (Planets)*, 117:E00L09, October 2012. doi: 10.1029/2012JE004161.
- S. J. Peale. Generalized Cassini’s Laws. *Astronom. J.*, 74:483, April 1969. doi: 10.1086/110825.
- S. A. Hauck, J.-L. Margot, S. C. Solomon, R. J. Phillips, C. L. Johnson, F. G. Lemoine, E. Mazarico, T. J. McCoy, S. Padovan, S. J. Peale, M. E. Perry, D. E. Smith, and M. T. Zuber. The curious case of Mercury’s internal structure. *Journal of Geophysical Research (Planets)*, 118:1204–1220, June 2013. doi: 10.1002/jgre.20091.
- A. Rivoldini and T. Van Hoolst. The interior structure of Mercury constrained by the low-degree gravity field and the rotation of Mercury. *Earth Planet. Sci. Lett.*, 377:62–72, September 2013. doi: 10.1016/j.epsl.2013.07.021.

- L. R. Nittler, R. D. Starr, S. Z. Weider, T. J. McCoy, W. V. Boynton, D. S. Ebel, C. M. Ernst, L. G. Evans, J. O. Goldsten, D. K. Hamara, D. J. Lawrence, R. L. McNutt, C. E. Schlemm, S. C. Solomon, and A. L. Sprague. The Major-Element Composition of Mercury’s Surface from MESSENGER X-ray Spectrometry. *Science*, 333:1847–, September 2011. doi: 10.1126/science.1211567.
- G. Di Achille, C. Popa, M. Massironi, E. Mazzotta Epifani, M. Zusi, G. Cremonese, and P. Palumbo. Mercury’s radius change estimates revisited using MESSENGER data. *Icarus*, 221:456–460, September 2012. doi: 10.1016/j.icarus.2012.07.005.
- M. Grott, D. Breuer, and M. Laneuville. Thermo-chemical evolution and global contraction of mercury. *Earth Planet. Sci. Lett.*, 307:135–146, July 2011. doi: 10.1016/j.epsl.2011.04.040.
- N. Tosi, M. Grott, A.C. Plesa, and D. Breuer. Thermochemical evolution of Mercury’s interior. acc. for pub. at *Geophys. Res. Lett.*, 2014.
- S. C. Solomon, P. K. Byrne, C. Klimczak, A. M. Cegal Sengor, T. R. Watters, and S. A. Hauck. Geological evidence that Mercury contracted by more than previously recognized. presented at AGU, Dec. 2013, 2014.
- N. C. Michel, S. A. Hauck, S. C. Solomon, R. J. Phillips, J. H. Roberts, and M. T. Zuber. Thermal evolution of Mercury as constrained by MESSENGER observations. *J. Geophys. Res.*, 118:1033–1044, May 2013. doi: 10.1002/jgre.20049.
- S. A. Hauck, J. M. Aurnou, and A. J. Dombard. Sulfur’s impact on core evolution and magnetic field generation on Ganymede. *J. Geophys. Res.*, 111:E09008, September 2006. doi: 10.1029/2005JE002557.
- A. Rivoldini, T. Van Hoolst, O. Verhoeven, A. Mocquet, and V. Dehant. Geodesy constraints on the interior structure and composition of Mars. *Icarus*, 213:451–472, June 2011. doi: 10.1016/j.icarus.2011.03.024.
- R. Vilim, S. Stanley, and S. A. Hauck. Iron snow zones as a mechanism for generating Mercury’s weak observed magnetic field. *J. Geophys. Res.*, 115(E14):E11003, November 2010. doi: 10.1029/2009JE003528.
- V. Malavergne, M. J. Toplis, S. Berthet, and J. Jones. Highly reducing conditions during core formation on Mercury: Implications for internal structure and the origin of a magnetic field. *Icarus*, 206:199–209, March 2010. doi: 10.1016/j.icarus.2009.09.001.
- G. Morard and T. Katsura. Pressure-temperature cartography of Fe-S-Si immiscible system. *Geoch. Cosmoch. Acta*, 74:3659–3667, June 2010. doi: 10.1016/j.gca.2010.03.025.
- J. Wicht, S. Stellmach, and H. Harder. Numerical dynamo simulations: From basic concepts to realistic models. In W. Freedman, M.Z. Nashed, and T. Sonar, editors, *Handbook of Geomathematics, sec. ed.*, pages 459–502. Springer, Berlin - Heidelberg - NewYork, 2011a.
- W. Dietrich and J. Wicht. A hemispherical dynamo model: Implications for the Martian crustal magnetization. *Phys. Earth Planet. Inter.*, 217:10–21, April 2013. doi: 10.1016/j.pepi.2013.01.001.
- S. Stanley, L. Elkins-Tanton, M. T. Zuber, and E. M. Parmentier. Mars’s Paleomagnetic Field as the Result of a Single-Hemisphere Dynamo. *Science*, 321:1822–, September 2008. doi: 10.1126/science.1161119.

- H. Amit, U. R. Christensen, and B. Langlais. The influence of degree-1 mantle heterogeneity on the past dynamo of Mars. *Phys. Earth Planet. Inter.*, 189:63–79, November 2011. doi: 10.1016/j.pepi.2011.07.008.
- B. W. Denevi, C. M. Ernst, H. M. Meyer, M. S. Robinson, S. L. Murchie, J. L. Whitten, J. W. Head, T. R. Watters, S. C. Solomon, L. R. Ostrach, C. R. Chapman, P. K. Byrne, C. Klimczak, and P. N. Peplowski. The distribution and origin of smooth plains on Mercury. *J. Geophys. Res.*, 118:891–907, May 2013. doi: 10.1002/jgre.20075.
- J.-P. Williams, J. Ruiz, M. A. Rosenburg, O. Aharonson, and R. J. Phillips. Insolation driven variations of Mercury’s lithospheric strength. *J. Geophys. Res.*, 116:E01008, January 2011. doi: 10.1029/2010JE003655.
- R. M. Winslow, B. J. Anderson, C. L. Johnson, J. A. Slavin, H. Korth, M. E. Purucker, D. N. Baker, and S. C. Solomon. Mercury’s magnetopause and bow shock from MESSENGER Magnetometer observations. *J. Geophys. Res.*, 118:2213–2227, May 2013. doi: 10.1002/jgra.50237.
- J. Müller, S. Simon, Y.-C. Wang, U. Motschmann, D. Heyner, J. Schüle, W.-H. Ip, G. Kleindienst, and G. J. Pringle. Origin of Mercury’s double magnetopause: 3D hybrid simulation study with A.I.K.E.F. *Icarus*, 218:666–687, March 2012. doi: 10.1016/j.icarus.2011.12.028.
- K.-H. Glassmeier, H.-U. Auster, D. Heyner, K. Okrafka, C. Carr, G. Berghofer, B. J. Anderson, A. Balogh, W. Baumjohann, P. Cargill, U. Christensen, M. Delva, M. Dougherty, K.-H. Fornacon, T. S. Horbury, E. A. Lucek, W. Magnes, M. Manda, A. Matsuoka, M. Matsushima, U. Motschmann, R. Nakamura, Y. Narita, H. O’Brien, I. Richter, K. Schwingenschuh, H. Shibuya, J. A. Slavin, C. Sotin, B. Stoll, H. Tsunakawa, S. Vennerstrom, J. Vogt, and T. Zhang. The fluxgate magnetometer of the BepiColombo Mercury Planetary Orbiter. *Planet. Space Sci.*, 58:287–299, January 2010. doi: 10.1016/j.pss.2008.06.018.
- J. A. Slavin, B. J. Anderson, D. N. Baker, M. Benna, S. A. Boardsen, R. E. Gold, G. C. Ho, S. M. Imber, H. Korth, S. M. Krimigis, R. L. McNutt, Jr., J. M. Raines, M. Sarantos, D. Schriver, S. C. Solomon, P. Trávníček, and T. H. Zurbuchen. MESSENGER and Mariner 10 flyby observations of magnetotail structure and dynamics at Mercury. *J. Geophys. Res.*, 117:A01215, January 2012. doi: 10.1029/2011JA016900.
- P. Janhunen and E. Kallio. Surface conductivity of Mercury provides current closure and may affect magnetospheric symmetry. *Annales Geophysicae*, 22:1829–1837, May 2004. doi: 10.5194/angeo-22-1829-2004.
- G. A. Dibraccio, J. A. Slavin, S. A. Boardsen, B. J. Anderson, H. Korth, T. H. Zurbuchen, J. M. Raines, D. N. Baker, R. L. McNutt, and S. C. Solomon. MESSENGER observations of magnetopause structure and dynamics at Mercury. *Journal of Geophysical Research (Space Physics)*, 118:997–1008, March 2013. doi: 10.1002/jgra.50123.
- W. Baumjohann, M. Blanc, A. Fedorov, and K.-H. Glassmeier. Current Systems in Planetary Magnetospheres and Ionospheres. *Space Sci. Rev.*, 152:99–134, May 2010. doi: 10.1007/s11214-010-9629-z.
- V. Mangano, S. Massetti, A. Milillo, A. Mura, S. Orsini, and F. Leblanc. Dynamical evolution of sodium anisotropies in the exosphere of Mercury. *Planet. Space Sci.*, 82:1–10, July 2013. doi: 10.1016/j.pss.2013.03.002.

- K.-H. Glassmeier, H.-U. Auster, and U. Motschmann. A feedback dynamo generating Mercury's magnetic field. *Geophys. Res. Lett.*, 34:22201–+, November 2007. doi: 10.1029/2007GL031662.
- J. Bartels. The eccentric dipole approximating the Earth's magnetic field. *J. Geophys. Res.*, 41:225–250, 1936.
- I. I. Alexeev, E. S. Belenkaya, J. A. Slavin, H. Korth, B. J. Anderson, D. N. Baker, S. A. Boardsen, C. L. Johnson, M. E. Purucker, M. Sarantos, and S. C. Solomon. Mercury's magnetospheric magnetic field after the first two MESSENGER flybys. *Icarus*, 209:23–39, September 2010. doi: 10.1016/j.icarus.2010.01.024.
- V. Lesur, P. Kunagu, S. Asari, M. Hamoudi, M. Rother, and I. Wardinski. GRIMM-3, Third version of the GFZ Reference Internal magnetic Model. In preparation, 2012.
- J. E. P. Connerney, M. H. Acuña, N. F. Ness, and T. Satoh. New models of Jupiter's magnetic field constrained by the Io flux tube footprint. *J. Geophys. Res.*, 103:11929–11940, June 1998. doi: 10.1029/97JA03726.
- H. Cao, C. T. Russell, J. Wicht, U. R. Christensen, and M. K. Dougherty. Saturn's high degree magnetic moments: evidence for a unique planetary dynamo. *Icarus*, 221:388–394, 2012.
- R. Holme and J. Bloxham. The magnetic fields of Uranus and Neptune: Methods and models. *J. Geophys. Res.*, 101:2177–2200, 1996. doi: 10.1029/95JE03437.
- M. E. Purucker, C. L. Johnson, R. M. Winslow, J. B. Nicholas, B. J. Anderson, H. Korth, J. W. Head, M. T. Zuber, S. C. Solomon, J. A. Slavin, I. I. Alexeev, R. J. Phillips, and D. A. Paige. Evidence for a Crustal Magnetic Signature on Mercury from MESSENGER Magnetometer Observations. In *Lunar and Planetary Institute Science Conference Abstracts*, volume 43 of *Lunar and Planetary Institute Science Conference Abstracts*, page 1297, March 2012.
- S.I. Braginsky and P.H. Roberts. Equations governing convection in Earth's core and the geodynamo. *Geophys. Astrophys. Fluid Dyn.*, 79:1–97, 1995.
- C. Kutzner and U.R. Christensen. Effects of driving mechanisms in geodynamo models. *Geophys. Res. Lett.*, 27:29–32, 2000.
- J. Aubert, H. Amit, G. Hulot, and P. Olson. Thermochemical flows couple the Earth's inner core growth to mantle heterogeneity. *Nature*, 454:758–761, August 2008. doi: 10.1038/nature07109.
- U. Christensen and J. Wicht. Numerical dynamo simulations. In Olson P., editor, *Core Dynamics*, volume 8 of *Treatise on Geophysics*, pages 245–282. Elsevier, 2007.
- J. Wicht, M. Mandea, F. Takahashi, U. R. Christensen, M. Matsushima, and B. Langlais. The Origin of Mercury's Internal Magnetic Field. *Space Sci. Rev.*, 132:261–290, October 2007. doi: 10.1007/s11214-007-9280-5.
- S. Stanley and G. A. Glatzmaier. Dynamo Models for Planets Other Than Earth. *Space Sci. Rev.*, 152:617–649, May 2010. doi: 10.1007/s11214-009-9573-y.
- G. Schubert and K. M. Soderlund. Planetary magnetic fields: Observations and models. *Phys. Earth Planet. Inter.*, 187:92–108, August 2011. doi: 10.1016/j.pepi.2011.05.013.

- P. Olson and U. Christensen. Dipole moment scaling for convection-driven planetary dynamos. *Earth Planet. Sci. Lett.*, 250:561–571, 2006.
- U. R. Christensen. Dynamo scaling laws: applications to the planets. *Space Sci. Rev.*, 152:565–590, 2010.
- J. Wicht, S. Stellmach, and H. Harder. Numerical dynamo simulations: From basic concepts to realistic models. In W. Freeden, M.Z. Nashed, and T. Sonar, editors, *Handbook of Geomathematics*, pages 459–502. Springer, Berlin - Heidelberg - NewYork, 2011b.
- U. R. Christensen, J. Aubert, and G. Hulot. Conditions for Earth-like geodynamo models. *Earth Planet. Sci. Lett.*, 296:487–496, August 2010. doi: 10.1016/j.epsl.2010.06.009.
- U. Christensen and J. Aubert. Scaling properties of convection-driven dynamos in rotating spherical shells and applications to planetary magnetic fields. *Geophys. J. Int.*, 116: 97–114, 2006.
- D. J. Stevenson. Saturn’s luminosity and magnetism. *Science*, 208:746–748, 1980.
- W. Lorenzen, B. Holst, and R. Redmer. Demixing of Hydrogen and Helium at Megabar Pressures. *Phys. Rev. Lett.*, 102(11):115701, March 2009. doi: 10.1103/PhysRevLett.102.115701.
- U. R. Christensen. A deep dynamo generating Mercury’s magnetic field. *Nature*, 444:1056–1058, 2006.
- U. R. Christensen and J. Wicht. Models of magnetic field generation in partly stable planetary cores: Applications to Mercury and Saturn. *Icarus*, 196:16–34, July 2008. doi: 10.1016/j.icarus.2008.02.013.
- U. Christensen and A. Tilgner. Power requirement of the geodynamo from Ohmic losses in numerical and laboratory dynamos. *Nature*, 429:169–171, 2004.
- F. Lhuillier, A. Fournier, G. Hulot, and J. Aubert. The geomagnetic secular variation timescale in observations and numerical dynamo models. *Geophys. Res. Lett.*, 38: L09306, 2011.
- A. Manglik, J. Wicht, and U. R. Christensen. A dynamo model with double diffusive convection for Mercury’s core. *Earth and Planetary Science Letters*, 289:619–628, January 2010. doi: 10.1016/j.epsl.2009.12.007.
- H. Cao, J. Aurnou, J. Wicht, W. Dietrich, K. M. Soderlund, and C. T. Russell. A dynamo explanation for the large offset of Mercury’s magnetic equator. submitted to *Geophys. Res. Lett.*, 2014.
- K. Hori, J. Wicht, and U. R. Christensen. The influence of thermo-compositional boundary conditions on convection and dynamos in a rotating spherical shell. *Phys. Earth Planet. Inter.*, 196:32–48, April 2012. doi: 10.1016/j.pepi.2012.02.002.
- M. Landeau and J. Aubert. Equatorially asymmetric convection inducing a hemispherical magnetic field in rotating spheres and implications for the past martian dynamo. *Physics of the Earth and Planetary Interiors*, 185:61–73, April 2011. doi: 10.1016/j.pepi.2011.01.004.
- Z. Tian, M. T. Zuber, and S. Stanley. Explaining Mercurys magnetic field observables using dynamo models with stable layers and laterally variable heat flux. presented at AGU, Dec. 2013, 2013.
- D. Heyner, J. Wicht, N. Gómez-Pérez, D. Schmitt, H.-U. Auster, and K.-H. Glass-

- meier. Evidence from Numerical Experiments for a Feedback Dynamo Generating Mercury's Magnetic Field. *Science*, 334:1690–, December 2011a. doi: 10.1126/science.1207290.
- M. H. Heimpel, J. M. Aurnou, F. M. Al-Shamali, and N. Gomez Perez. A numerical study of dynamo action as a function of spherical shell geometry. *Earth Planet. Sci. Lett.*, 236:542–557, July 2005. doi: 10.1016/j.epsl.2005.04.032.
- F. Takahashi and M. Matsushima. Dipolar and non-dipolar dynamos in a thin shell geometry with implications for the magnetic field of Mercury. *Geophys. Res. Lett.*, 33:L10202, 2006. doi: 10.1029/2006GL025792.
- S. Stanley, J. Bloxham, W.E. Hutchison, and M.T. Zuber. Thin shell dynamo models consistent with Mercury's weak observed magnetic field. *Earth Planet. Sci. Lett.*, 234:341–353, 2005.
- D. Heyner, D. Schmitt, J. Wicht, K.-H. Glassmeier, H. Korth, and U. Motschmann. The initial temporal evolution of a feedback dynamo for Mercury. *Geophys. Astrophys. Fluid Dyn.*, 104:419–429, August 2010. doi: 10.1080/03091921003776839.
- D. Heyner, D. Schmitt, K.-H. Glassmeier, and J. Wicht. Dynamo action in an ambient field. *Astronom. Nach.*, 332:36, January 2011b. doi: 10.1002/asna.201011466.